INTERNATIONAL JOURNAL FOR NUMERICAL METHODS IN ENGINEERING

Int. J. Numer. Meth. Engng 2014; **1**:1–44 *Prepared using* nmeauth.cls *[Version: 2000/01/19 v2.0]*

Consistent and stable meshfree Galerkin methods using the virtual element decomposition

A. Ortiz-Bernardin[1,*], A. Russo[2,3] and N. Sukumar[4]

[1] *Department of Mechanical Engineering, University of Chile, Av. Beauchef 851, Santiago 8370456, Chile.*

[2] *Dipartimento di Matematica e Applicazioni, Università di Milano-Bicocca, 20153 Milano, Italy*

[3] *Istituto di Matematica Applicata e Tecnologie Informatiche del CNR, via Ferrata 1, 27100 Pavia, Italy,*

[4] *Department of Civil and Environmental Engineering, University of California, Davis, CA 95616, USA*

SUMMARY

Over the past two decades, meshfree methods have undergone significant development as a numerical tool to solve partial differential equations (PDEs). In contrast to finite elements, the basis functions in meshfree method are smooth (nonpolynomial functions), and they do not rely on an underlying mesh structure for their construction. These features render meshfree methods to be particularly appealing for higher-order PDEs and for large deformation simulations of solid continua. However, a deficiency that still persists in meshfree Galerkin methods is the inaccuracies in numerical integration, which affects the consistency and stability of the method. Several previous contributions have tackled the issue of integration errors with an eye on consistency, but without explicitly ensuring stability. In this paper, we draw on the recently proposed virtual element method, to present a formulation that guarantees both the consistency and stability of the approximate bilinear form. We adopt maximum-entropy meshfree basis functions, but other meshfree basis

*Correspondence to: A. Ortiz-Bernardin, Department of Mechanical Engineering, University of Chile, Av. Beauchef 851, Santiago 8370456, Chile. E-mail: aortizb@ing.uchile.cl

functions can also be used within this framework. Numerical results for several two- and three-dimensional elliptic (Poisson and linear elastostatic) boundary-value problems that demonstrate the effectiveness of the proposed formulation are presented.

KEY WORDS: meshfree Galerkin methods, maximum-entropy approximants, numerical integration, virtual element method, patch test, stability

1. INTRODUCTION

Meshfree methods [1, 2] that are built from a weak form (referred to as meshfree Galerkin methods) require background integration cells on which the numerical integration of the weak form integrals is carried out. Typically, the domain of an integration cell does not coincide with the region that is defined by the intersecting supports of two overlapping meshfree basis functions. In addition, meshfree basis functions are nonpolynomial functions. These are two key observations that introduce integration errors when standard Gauss quadrature is used to numerically integrate the stiffness matrix in meshfree Galerkin methods. As a consequence, the consistency, optimal convergence, and even stability in some instances of the numerical solution can be compromised. In this paper, we present a new methodology — based on the decomposition of the bilinear form in the virtual element method [3] — for the numerical integration of the stiffness matrix that precludes integration errors when using integration cells that are obtained from a Delaunay tessellation. Furthermore, this ensures that the meshfree Galerkin method is, both, consistent and stable.

Quadrature errors in meshfree Galerkin methods lead to consistency errors (patch test is not passed), and underintegration can also compromise the stability of the method. In the literature, various approaches have been put forth to address errors due to numerical integration. The interested reader is referred to Reference [4], where more details are provided on the topic of

numerical integration in meshfree methods. Herein, we only mention pertinent studies that have attempted to correct the integration errors. Babuška and coworkers have provided the theoretical basis for the issue that arises in the numerical integration of first-order meshfree methods [5] as well as higher-order meshfree approximations [6]. With the aim of satisfying the patch test, use of a smoothed strain operator [7] was first adopted in nodally integrated meshfree methods by Chen et al. [8]. Breitkopf et al. [9] developed a custom integration scheme for the diffuse element method [10] based on the ideas drawn by Chen et al. to ensure patch test satisfaction. Ortiz et al. [11] proposed a strain-correction based on a smoothing procedure for linear approximations on triangular and quadrilateral background meshes and extended these ideas to tetrahedral background meshes in Reference [12]. A similar idea is used to correct integration errors in polygonal and polyhedral finite element methods [13]. Chen et al. [4] proposed a variationally consistent integration method for higher-order meshfree approximations that generalizes the notion of nodal integration and is applicable for Gauss quadrature within triangles and squares. Duan et al. [14] proposed a smoothing procedure for second-order approximations on triangular background meshes, and have used to the Hu-Washizu three-field variational principle to shown the variational consistency of the integration scheme on triangular meshes [15]. The corresponding second-order accurate integration scheme for four-node tetrahedral meshes is presented in Reference [16]. On adopting the techniques of Duan et al. [15, 16], Ortiz-Bernardin and coworkers [17, 18] presented formulations to treat nearly-incompressible elasticity in the small- and finite-deformation regimes. All these aforementioned integration methods are developed to remove the consistency error from the numerical solution; none of them theoretically guarantee stability.

Recently, the virtual element method [3] (VEM) has been presented, where an algebraic (exact) construction of the stiffness matrix is realized without the explicit construction of basis

functions (basis functions are *virtual*). In the VEM, the stiffness matrix is decomposed into two parts: a consistent term that reproduces a given polynomial space and a correction term that provides stability. Such a decomposition (herein referred to as the *virtual element decomposition*) is formulated in the spirit of the Lax equivalence theorem (consistency + stability $\rightarrow$ convergence) for finite-difference schemes and is sufficient for the method to pass the patch test [19].

The formulation in the virtual element method constitutes a suitable framework to correct integration errors in meshfree methods. Talischi and Paulino [20] and Manzini et al. [21] have applied these concepts to ameliorate numerical integration errors in polygonal and polyhedral finite elements. In this paper, we follow similar ideas for meshfree methods and adopt the virtual element decomposition to construct the stiffness matrix, which ensures both consistency and stability of the solution. We note in passing that meshfree nodal integration methods, which require corrections to ensure consistency and stability [8, 22–25], can likely also be formulated using the virtual element framework. Maximum-entropy basis functions [26–28] are adopted to exemplify our procedure (see Section 2), though other meshfree basis functions can also be used in this approach. The governing equations for elliptic (Poisson and linear elastostatic) boundary-value problems are summarized in Section Section 3. The methodology to construct the stiffness matrix using meshfree basis functions and the virtual element decomposition is presented in Section 4. Delaunay tessellations (three-node triangles and four-node tetrahedra) are considered to obtain the nodal information for basis functions computation and for numerical integration. In Section 5, it is shown how the patch test is satisfied for the proposed method. Numerical examples for two- and three-dimensional Poisson and linear elastostatic problems and eigenvalue analyses are presented in Section 6, which demonstrate the consistency, stability and effectiveness of the proposed formulation. We close with some final remarks in Section 7.

2. MAXIMUM-ENTROPY BASIS FUNCTIONS

Consider a convex domain represented by a set of n scattered nodes and a prior (weight) function $w_a(\boldsymbol{x})$ associated with each node a. We can write down the approximation for a scalar-valued function $u(\boldsymbol{x})$ in the form:

$$u(\boldsymbol{x}) = \sum_{a=1}^{m} \phi_a(\boldsymbol{x}) u(\boldsymbol{x}_a), \tag{1}$$

where $u(\boldsymbol{x}_a)$ are nodal coefficients. On using the Shannon-Jaynes (or relative) entropy functional, the max-ent basis functions $\{\phi_a(\boldsymbol{x}) \geq 0\}_{a=1}^{m}$ are obtained via the solution of the following convex optimization problem [28]:

$$\min_{\boldsymbol{\phi} \in \mathbb{R}_+^m} \sum_{a=1}^{m} \phi_a(\boldsymbol{x}) \ln\left(\frac{\phi_a(\boldsymbol{x})}{w_a(\boldsymbol{x})}\right) \tag{2a}$$

subject to the linear reproducing conditions:

$$\sum_{a=1}^{m} \phi_a(\boldsymbol{x}) = 1 \quad \sum_{a=1}^{m} \phi_a(\boldsymbol{x})\, \boldsymbol{c}_a = \boldsymbol{0}, \tag{2b}$$

where $\boldsymbol{c}_a = \boldsymbol{x}_a - \boldsymbol{x}$ are shifted nodal coordinates and $\mathbb{R}_+^m$ is the nonnegative orthant. In this paper, we use as the prior weight function the Gaussian radial basis function given by [27]

$$w_a(\boldsymbol{x}) = \exp\left(-\frac{\gamma}{h_a^2}\|\boldsymbol{c}_a\|^2\right),$$

where γ is a parameter that controls the support size of the basis function and h_a is a characteristic nodal spacing associated with node a.

On using the method of Lagrange multipliers, the solution to (2) is given by [28]

$$\phi_a(\boldsymbol{x}, \boldsymbol{\lambda}) = \frac{w_a(\boldsymbol{x}) \exp(-\boldsymbol{\lambda}(\boldsymbol{x}) \cdot \boldsymbol{c}_a(\boldsymbol{x}))}{Z(\boldsymbol{x}, \boldsymbol{\lambda}(\boldsymbol{x}))}, \quad Z(\boldsymbol{x}, \boldsymbol{\lambda}(\boldsymbol{x})) = \sum_{b=1}^{m} w_b(\boldsymbol{x}) \exp(-\boldsymbol{\lambda}(\boldsymbol{x}) \cdot \boldsymbol{c}_b(\boldsymbol{x})), \tag{3}$$

where the Lagrange multiplier vector $\boldsymbol{\lambda}(\boldsymbol{x})$ is obtained as the minimizer of the dual optimization problem ($\boldsymbol{x}$ is fixed):

$$\boldsymbol{\lambda}^*(\boldsymbol{x}) = \arg\min_{\boldsymbol{\lambda} \in \mathbb{R}^d} \ln Z(\boldsymbol{x}, \boldsymbol{\lambda}),$$

Prepared using nmeauth.cls

where $\boldsymbol{\lambda}^*$ is the converged solution for the Lagrange multiplier vector. The basis functions $\phi_a(\boldsymbol{x})$ are obtained by using $\boldsymbol{\lambda} = \boldsymbol{\lambda}^*$ in (3). Finally, the gradient of the basis function is [27]:

$$\nabla\phi_a(\boldsymbol{x}) = \phi_a(\boldsymbol{x}, \boldsymbol{\lambda}^*)\,(J(\boldsymbol{x}, \boldsymbol{\lambda}^*))^{-1}\,\boldsymbol{c}_a(\boldsymbol{x}),$$

where

$$J(\boldsymbol{x}, \boldsymbol{\lambda}) = \sum_{a=1}^{m} \phi_a(\boldsymbol{x}, \boldsymbol{\lambda})\,\boldsymbol{c}_a(\boldsymbol{x}) \otimes \boldsymbol{c}_a(\boldsymbol{x}) - \boldsymbol{r}(\boldsymbol{x}, \boldsymbol{\lambda}) \otimes \boldsymbol{r}(\boldsymbol{x}, \boldsymbol{\lambda}), \quad \boldsymbol{r}(\boldsymbol{x}, \boldsymbol{\lambda}) = -\sum_{a=1}^{m} \phi_a(\boldsymbol{x}, \boldsymbol{\lambda})\,\boldsymbol{c}_a(\boldsymbol{x}).$$

3. GOVERNING EQUATIONS

The numerical solution of two boundary-value problems are considered: Poisson problem with nonhomogeneous Dirichlet boundary conditions and linear elastostatics. The field variables in both problems are discretized using meshfree (maximum-entropy) basis functions that span the space of linear polynomials.

3.1. Poisson problem

Consider an open bounded domain $\Omega \subset \mathbb{R}^d$ $(d = 2, 3)$ that is bounded by the $(d-1)$-dimensional surface Γ whose unit outward normal is $\boldsymbol{n}$. The Dirichlet boundary is denoted by Γ_g. The closure of the domain is $\overline{\Omega} \equiv \Omega \cup \Gamma$. Let $u(\boldsymbol{x}) : \Omega \to \mathbb{R}$ be the field variable and $f(\boldsymbol{x}) : \Omega \to \mathbb{R}$ be the source term. The imposed Dirichlet (essential) boundary conditions are $g(\boldsymbol{x}) : \Gamma_g \to \mathbb{R}$. The boundary-value problem that governs the Poisson problem is: find $u(\boldsymbol{x}) : \Omega \to \mathbb{R}$ such that

$$-\boldsymbol{\nabla}^2 u = f \quad \forall \boldsymbol{x} \in \Omega, \tag{4a}$$

$$u = g \quad \forall \boldsymbol{x} \in \Gamma_g. \tag{4b}$$

The corresponding weak form is: find $u(\boldsymbol{x}) \in \mathscr{U}$ such that

$$a(u, v) = \ell(v) \quad \forall v(\boldsymbol{x}) \in \mathscr{V}, \quad a(u, v) = \int_\Omega \boldsymbol{\nabla} u \cdot \boldsymbol{\nabla} v \, d\boldsymbol{x}, \quad \ell(v) = \int_\Omega f v \, d\boldsymbol{x}, \tag{5}$$

where $\mathscr{U}$ and $\mathscr{V}$ are the trial and test spaces:

$$\mathscr{U} := \left\{ u(\boldsymbol{x}) : u \in \mathcal{W}(\Omega) \subseteq H^1(\Omega),\ u = g \text{ on } \Gamma_g \right\},$$

$$\mathscr{V} := \left\{ v(\boldsymbol{x}) : v \in \mathcal{W}(\Omega) \subseteq H^1(\Omega),\ v = 0 \text{ on } \Gamma_g \right\},$$

where the space $\mathcal{W}(\Omega)$ includes affine functions. In the weak form (5), we substitute trial and test functions of the form given in (1), and apply a standard Galerkin procedure to obtain the following system of linear equations:

$$\boldsymbol{K}\boldsymbol{d} = \boldsymbol{f}, \qquad \boldsymbol{K}_{ab} = \int_\Omega \boldsymbol{\nabla}\phi_a \cdot \boldsymbol{\nabla}\phi_b \, d\boldsymbol{x}, \qquad \boldsymbol{f}_a = \int_\Omega f\phi_a \, d\boldsymbol{x}, \tag{7}$$

where $\boldsymbol{K}$ is the stiffness matrix, $\boldsymbol{f}$ the nodal force vector, and $\boldsymbol{d}$ is the vector of nodal coefficients associated with the field variable.

3.2. Linear elastostatic boundary-value problem

Consider an elastic body that occupies the open domain $\Omega \subset \mathbb{R}^d$ $(d = 2, 3)$ and is bounded by the $(d-1)$-dimensional surface Γ whose unit outward normal is $\boldsymbol{n}$. The boundary is assumed to admit decompositions $\Gamma = \Gamma_g \cup \Gamma_h$ and $\emptyset = \Gamma_g \cap \Gamma_h$, where Γ_g is the Dirichlet boundary and Γ_h is the Neumann boundary. The closure of the domain is $\overline{\Omega} \equiv \Omega \cup \Gamma$. Let $\boldsymbol{u}(\boldsymbol{x}) : \Omega \to \mathbb{R}^d$ be the displacement field at a point $\boldsymbol{x}$ of the elastic body when the body is subjected to external tractions $\boldsymbol{h}(\boldsymbol{x}) : \Gamma_h \to \mathbb{R}^d$ and body forces $\boldsymbol{b}(\boldsymbol{x}) : \Omega \to \mathbb{R}^d$. The imposed Dirichlet (essential) boundary conditions are $\boldsymbol{g}(\boldsymbol{x}) : \Gamma_g \to \mathbb{R}^d$. The boundary-value problem for linear elastostatics is: find $\boldsymbol{u}(\boldsymbol{x}) : \Omega \to \mathbb{R}^d$ such that

$$\boldsymbol{\nabla} \cdot \boldsymbol{\sigma} + \boldsymbol{b} = 0 \quad \forall \boldsymbol{x} \in \Omega, \tag{8a}$$

$$\boldsymbol{u} = \boldsymbol{g} \quad \forall \boldsymbol{x} \in \Gamma_g, \tag{8b}$$

$$\boldsymbol{\sigma} \cdot \boldsymbol{n} = \boldsymbol{h} \quad \forall \boldsymbol{x} \in \Gamma_h, \tag{8c}$$

where $\boldsymbol{\sigma}$ is the Cauchy stress tensor. The corresponding weak form is: find $\boldsymbol{u}(\boldsymbol{x}) \in \mathscr{U}$ such that

$$a(\boldsymbol{u},\boldsymbol{v}) = \ell(\boldsymbol{v}) \quad \forall \boldsymbol{v}(\boldsymbol{x}) \in \mathscr{V}, \quad a(\boldsymbol{u},\boldsymbol{v}) = \int_{\Omega} \boldsymbol{\sigma}(\boldsymbol{u}) : \boldsymbol{\varepsilon}(\boldsymbol{v})\, d\boldsymbol{x}, \quad \ell(\boldsymbol{v}) = \int_{\Omega} \boldsymbol{b}\cdot\boldsymbol{v}\, d\boldsymbol{x} + \int_{\Gamma_h} \boldsymbol{h}\cdot\boldsymbol{v}\, dS, \tag{9}$$

where $\boldsymbol{\varepsilon}$ is the small strain tensor, and $\mathscr{U}$ and $\mathscr{V}$ are the displacement trial and test spaces:

$$\mathscr{U} := \left\{ \boldsymbol{u}(\boldsymbol{x}) : \boldsymbol{u} \in [\mathcal{W}(\Omega)]^d \subseteq [H^1(\Omega)]^d,\ \boldsymbol{u} = \boldsymbol{g} \text{ on } \Gamma_g \right\},$$

$$\mathscr{V} := \left\{ \boldsymbol{v}(\boldsymbol{x}) : \boldsymbol{v} \in [\mathcal{W}(\Omega)]^d \subseteq [H^1(\Omega)]^d,\ \boldsymbol{v} = \boldsymbol{0} \text{ on } \Gamma_g \right\},$$

where the space $\mathcal{W}(\Omega)$ includes linear displacement fields. We substitute vector-valued trial and test functions of the form (1) into (9), and apply a standard Galerkin procedure to obtain the following system of linear equations:

$$\boldsymbol{K}\boldsymbol{d} = \boldsymbol{f}, \qquad \boldsymbol{K}_{ab} = \int_{\Omega} \boldsymbol{B}_a^{\mathrm{T}} \boldsymbol{C} \boldsymbol{B}_b\, d\boldsymbol{x}, \qquad \boldsymbol{f}_a = \int_{\Omega} \phi_a \boldsymbol{b}\, d\boldsymbol{x} + \int_{\Gamma_h} \phi_a \boldsymbol{h}\, dS, \tag{11}$$

where $\boldsymbol{K}$ is the stiffness matrix, $\boldsymbol{f}$ the nodal force vector, $\boldsymbol{d}$ the vector of nodal coefficients associated with the displacement field, $\boldsymbol{C}$ is the constitutive matrix for an isotropic linear elastic material, and $\boldsymbol{B}_a$ is the nodal matrix of basis function derivatives.

4. VIRTUAL ELEMENT DECOMPOSITION

Galerkin meshfree methods typically provide better convergence properties and smoother solutions than standard finite elements. However, in meshfree methods the numerical integration of the stiffness matrix using Gauss quadrature leads to inaccuracies that deteriorate the consistency and asymptotic convergence of the solution. If the solution to a problem that is governed by (4) or (8) is a linear polynomial, consistency means that the numerical solution must exactly reproduce the linear polynomial. On the other hand, insufficient number of quadrature points can compromise the stability of the method. Currently, there are integration schemes for meshfree methods that

recover the consistency of the solution (for example, see Chen et al. [4], Duan et al. [15, 16], Ortiz et al. [11, 12]) but none of them resolves the stability issue from a theoretical perspective. The virtual element decomposition [3, 29] constitutes a sound theoretical basis that can be used to construct a stiffness matrix that is consistent and stable. In the method that is proposed herein, the unknowns are solved using (7) or (11), but the stiffness matrix is constructed using the virtual element decomposition.

The essential features of the virtual element decomposition are presented; the exposition closely follows the notation and description in Gain et al. [30]. Let the domain Ω be partitioned into nonoverlapping integration cells. In this paper, the cells are restricted to be three-node triangles or four-node tetrahedra. An integration cell is denoted by E and its volume by $|E|$. The boundary of the integration cell is dS and the normal to this boundary is $\boldsymbol{n}_E = [n_1^E \quad n_2^E \quad n_3^E]^{\mathrm{T}}$. The mean value of a function h over the vertices of the integration cell is defined as

$$\bar{h} = \frac{1}{N}\sum_{J=1}^{N} h(\boldsymbol{x}_J), \tag{12}$$

where N is the number of nodes that define the integration cell whose vertex nodes have coordinates $\boldsymbol{x}_J$. For instance, $\bar{\boldsymbol{x}} = [\bar{x}_1 \quad \bar{x}_2 \quad \bar{x}_3]^{\mathrm{T}}$ is the geometric center of the integration cell. The partition of the domain is denoted by $\mathcal{T}$ so that each cell $E \in \mathcal{T}$. Note that on using this partitioning, the bilinear form given in (5) or (9) can be written as the following summation:

$$a(\alpha, \beta) = \sum_{E\in\mathcal{T}} a_E(\alpha, \beta), \tag{13}$$

where $\alpha = u$ and $\beta = v$ for the Poisson problem, and $\alpha = \boldsymbol{u}$ and $\beta = \boldsymbol{v}$ for the linear elastostatic boundary-value problem. In the virtual element decomposition, the stiffness matrix is constructed on each cell $E \in \mathcal{T}$ using projection operators.

4.1. Poisson problem

4.1.1. Projection operator. For the Poisson problem, a single projection operator is needed. For the construction of this operator, we denote the space of affine functions by $\mathcal{P}(E)$. As a consequence of using meshfree basis functions to construct the trial function, the scalar-field is composed of a (linear) polynomial part plus some additional nonpolynomial part, which implies that $u(\boldsymbol{x}) \in \mathcal{W}(E) \supseteq \mathcal{P}(E)$. Now, a projection operator Π that allows to extract the polynomial part of the field $u(\boldsymbol{x}) \in \mathcal{W}(E)$ is defined as follows:

$$\Pi : \mathcal{W}(E) \to \mathcal{P}(E), \quad \Pi p = p \quad \forall p \in \mathcal{P}(E). \tag{14}$$

In addition, it is required that Π satisfies the following orthogonality condition [3]:

$$a_E(u - \Pi u, p) = 0 \quad \forall p \in \mathcal{P}(E), \quad u \in \mathcal{W}(E), \tag{15}$$

which means that the nonpolynomial part $u - \Pi u$ is energetically orthogonal to $\mathcal{P}$.

An exact decomposition of an arbitrary u into a polynomial part and a nonpolynomial part is:

$$u = \Pi u + (u - \Pi u),$$

which after substituted into the bilinear form associated with a representative integration cell (see (13)) yields

$$\begin{aligned} a_E(u, v) &= a_E(\Pi u + (u - \Pi u), \Pi v + (v - \Pi v)) \\ &= a_E(\Pi u, \Pi v) + a_E(u - \Pi u, v - \Pi v) + a_E(u - \Pi u, \Pi v) + a_E(\Pi u, v - \Pi v) \\ &= a_E(\Pi u, \Pi v) + a_E(u - \Pi u, v - \Pi v), \end{aligned} \tag{16}$$

where we have used $a_E(u - \Pi u, \Pi v) = a_E(\Pi u, v - \Pi v) = 0$ due to the orthogonality condition (15). The first term on the right-hand side of the last equality in (16) provides consistency and the second term stability. A clear separation of the consistency and stabilization terms is the missing ingredient in existing integration schemes for meshfree methods [4, 11, 12, 15, 16].

A projection map that satisfies (14) and (15) is [31]:

$$\Pi u = \bar{u}s_0 + \hat{u}_{,1}s_1 + \hat{u}_{,2}s_2 + \hat{u}_{,3}s_3, \tag{17a}$$

$$\hat{u}_{,i} = \frac{1}{|E|}\int_{\partial E} un_i^E \, dS, \tag{17b}$$

where $\bar{u}$ is computed using (12), and $s_0, \ldots, s_3$ are the components of a scaled basis for the space of affine functions given by $\boldsymbol{s} = [1 \quad x_1 - \bar{x}_1 \quad x_2 - \bar{x}_2 \quad x_3 - \bar{x}_3]^{\mathrm{T}}$. The rationale for the specific choice given in (17a) for the projection operator is presented in Appendix A.

4.1.2. Stiffness matrix. To facilitate the understanding of the use of the virtual element decomposition to construct the meshfree stiffness matrix, the virtual element partitioning into cells needs to be placed within the meshfree context. In meshfree methods, the partitioned domain is used for two purposes: to obtain the nodal coordinates to compute the meshfree basis functions and to provide a suitable domain to perform the numerical integration of the weak form integrals. Therefore, if the cell-centric viewpoint of the virtual element decomposition is to be adopted for these purposes, then nodal basis functions of nodes that are outside a cell will contribute to the trial function space associated to this cell. The connection between the virtual element partitioning and the meshfree approximation is achieved through the definition of a nodal contribution[†] that represents the entire integration cell.

On each integration cell E, two types of Gauss points are considered: volume Gauss points that are defined in the interior of the cell and surface Gauss points that are defined on the cell faces. In some instances, we will use both types of Gauss points and in others only the surface Gauss points. Each of these Gauss points has its own nodal contribution. We merge these independent

[†]The nodal contribution at a given sampling point (usually a Gauss point) with coordinate $\boldsymbol{x}$ is defined as the indices of the nodes whose basis functions have a nonzero value at $\boldsymbol{x}$.

nodal contributions into one larger structure that is representative of the entire cell. The local nodal indices in the merged nodal contribution are labelled from 1 to m. The coordinates of a representative node in the merged nodal contribution is denoted by $\boldsymbol{x}_a = [x_{1a} \quad x_{2a} \quad x_{3a}]^{\mathrm{T}}$. Figure 1 illustrates the construction of the merged nodal contribution for a three-node triangular cell when both types of Gauss points are used.

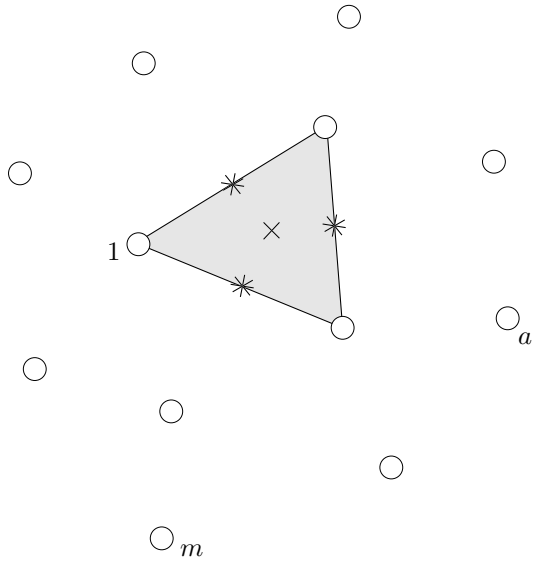

Figure 1: Schematic representation of the construction of the merged nodal contribution for a three-node triangular cell. The volume Gauss point is shown as a $\times$ and the boundary Gauss points as $*$. The nodes shown (open circles) are those nodes of the mesh that contribute within the triangle. The local index of the first node in the nodal contribution is labelled as 1 and the index of the last node as m. A representative node in the nodal contribution is labelled as a.

To obtain the consistent and stable stiffness matrices, we begin by writing the trial (or test)

approximation of a scalar-valued function within each integration cell as a linear combination of max-ent basis functions:

$$u^h(\boldsymbol{x}) = \sum_{a=1}^{m} \phi_a(\boldsymbol{x}) u_a, \tag{18}$$

where u_a are nodal coefficients. The max-ent basis functions are also used to represent the scaled basis for the space of affine functions, as follows:

$$\boldsymbol{s}^h(\boldsymbol{x}) = \sum_{a=1}^{m} \phi_a(\boldsymbol{x}) \boldsymbol{s}(\boldsymbol{x}_a). \tag{19}$$

The discrete version of the projection map to extract the polynomial part is obtained by substituting (18) and (19) into (17a), which yields

$$\Pi u^h = \boldsymbol{N}\boldsymbol{P}\boldsymbol{d},$$

where

$$\boldsymbol{N} = [\phi_1 \quad \cdots \quad \phi_a \quad \cdots \quad \phi_m], \quad \boldsymbol{d} = [u_1 \quad \cdots \quad u_a \quad \cdots \quad u_m]^{\mathrm{T}}$$

and

$$\boldsymbol{P} = \boldsymbol{H}\boldsymbol{W}^{\mathrm{T}},$$

with

$$\boldsymbol{H} = \begin{bmatrix} (\boldsymbol{H})_1 \\ \vdots \\ (\boldsymbol{H})_a \\ \vdots \\ (\boldsymbol{H})_m \end{bmatrix}, \quad (\boldsymbol{H})_a = \begin{bmatrix} 1 & x_{1a} - \bar{x}_1 & x_{2a} - \bar{x}_2 & x_{3a} - \bar{x}_3 \end{bmatrix}$$

and

$$\boldsymbol{W} = \begin{bmatrix} (\boldsymbol{W})_1 \\ \vdots \\ (\boldsymbol{W})_a \\ \vdots \\ (\boldsymbol{W})_m \end{bmatrix}, \; (\boldsymbol{W})_a = \begin{bmatrix} \bar{\phi}_a & 2q_{1a} & 2q_{2a} & 2q_{3a} \end{bmatrix}, \; q_{ia} = \frac{1}{2|E|} \int_{\partial E} \phi_a n_i^E \, dS.$$

It is noted that q_{ia} is computed approximately by using 1-point Gauss quadrature on the cell face since the meshfree basis function cannot be integrated exactly.

For the Poisson problem, the discrete version of the bilinear form is given by the virtual element decomposition on each cell (see (16)) as:

$$\begin{aligned} a_E(u^h, v^h) &= a_E(\Pi u^h, \Pi v^h) + a_E(u^h - \Pi u^h, v^h - \Pi v^h) \\ &= \boldsymbol{v}^{\mathrm{T}} \boldsymbol{W} \boldsymbol{H}^{\mathrm{T}} \, a_E(\boldsymbol{N}^{\mathrm{T}}, \boldsymbol{N}) \, \boldsymbol{H} \boldsymbol{W}^{\mathrm{T}} \boldsymbol{d} + \boldsymbol{v}^{\mathrm{T}} (\boldsymbol{I}_m - \boldsymbol{P})^{\mathrm{T}} \, a_E(\boldsymbol{N}^{\mathrm{T}}, \boldsymbol{N}) \, (\boldsymbol{I}_m - \boldsymbol{P}) \boldsymbol{d} \\ &= \boldsymbol{v}^{\mathrm{T}} \boldsymbol{W} \boldsymbol{H}^{\mathrm{T}} \boldsymbol{K} \boldsymbol{H} \boldsymbol{W}^{\mathrm{T}} \boldsymbol{d} + \boldsymbol{v}^{\mathrm{T}} (\boldsymbol{I}_m - \boldsymbol{P})^{\mathrm{T}} \boldsymbol{K} (\boldsymbol{I}_m - \boldsymbol{P}) \boldsymbol{d}, \end{aligned} \tag{20}$$

where $\boldsymbol{I}_m$ is the identity $(m \times m)$ matrix, with m being the number of nodes that contribute in the cell, $\boldsymbol{K}$ is the exact stiffness matrix, and $\boldsymbol{v}$ is a vector of arbitrary nodal coefficients that is associated with the scalar test function.

By observing that the projection can be written as $\Pi u^h = \boldsymbol{W} \boldsymbol{d} \boldsymbol{s}$, the consistency term in (20) can be developed as

$$a_E(\Pi u^h, \Pi v^h) = \boldsymbol{v}^{\mathrm{T}} \boldsymbol{W} \, a_E(\boldsymbol{s}^{\mathrm{T}}, \boldsymbol{s}) \, \boldsymbol{W}^{\mathrm{T}} \boldsymbol{d}, \tag{21}$$

where $a_E(\boldsymbol{s}^{\mathrm{T}}, \boldsymbol{s}) = \boldsymbol{I}_c|E|$ with

$$\boldsymbol{I}_c = \begin{bmatrix} 0 & 0 & 0 & 0 \\ 0 & 1 & 0 & 0 \\ 0 & 0 & 1 & 0 \\ 0 & 0 & 0 & 1 \end{bmatrix},$$

and thus the computation of (21) involves only the evaluation of few meshfree basis functions on the boundary of the cell — their derivatives are not needed. As pointed out in Reference [21], the exact stiffness matrix that appears in the second term on the right-hand side of the last equality in (20) can be replaced by an approximate stiffness without compromising the stability but gaining efficiency in the computations. In particular, we choose the approach adopted in Reference [21] and thus compute an approximate stiffness using 1-point Gauss quadrature on simplicial cells, which we denote by $\boldsymbol{K}_E^g$. Other options for the stiffness matrix in the stability term are possible and will be discussed in Section 4.2. On replacing $\boldsymbol{K}$ by $\boldsymbol{K}_E^g$ in the second term in (20), the final expression for the stiffness matrix associated with the integration cell is:

$$\boldsymbol{K}_E = |E|\boldsymbol{W}\boldsymbol{I}_c\boldsymbol{W}^{\mathrm{T}} + (\boldsymbol{I}_m - \boldsymbol{P})^{\mathrm{T}}\boldsymbol{K}_E^g(\boldsymbol{I}_m - \boldsymbol{P}).$$

4.2. Linear elastostatics

4.2.1. Projection operators. For the construction of the projection operators in linear elastostatics, three spaces are defined [30]: the space of rigid body motions (denoted by $\mathcal{R}$), the space of constant strain modes (denoted by $\mathcal{C}$), and the space of linear displacement (denoted by $\mathcal{P}$) that is able to represent rigid body motions and states of constant strains. The trial displacement field is composed of a (linear) polynomial part plus an additional nonpolynomial part, which implies that $\boldsymbol{u}(\boldsymbol{x}) \in [\mathcal{W}(E)]^d \supseteq [\mathcal{P}(E)]^d$.

Three projection operators are constructed to allow the extraction of rigid body motions, constant

strain modes and the polynomial part of any displacement field $\boldsymbol{u}(\boldsymbol{x}) \in \mathcal{W}(E)$ as follows:

$$\Pi_{\mathcal{R}} : [\mathcal{W}(E)]^d \to [\mathcal{R}(E)]^d, \quad \Pi_{\mathcal{R}}\boldsymbol{r} = \boldsymbol{r}, \quad \forall \boldsymbol{r} \in [\mathcal{R}(E)]^d \tag{22}$$

for extracting the rigid body motions,

$$\Pi_{\mathcal{C}} : [\mathcal{W}(E)]^d \to [\mathcal{C}(E)]^d, \quad \Pi_{\mathcal{C}}\boldsymbol{c} = \boldsymbol{c}, \quad \forall \boldsymbol{c} \in [\mathcal{C}(E)]^d \tag{23}$$

for extracting the constant strain modes, and

$$\Pi_{\mathcal{P}} : [\mathcal{W}(E)]^d \to [\mathcal{P}(E)]^d, \quad \Pi_{\mathcal{P}}\boldsymbol{p} = \boldsymbol{p}, \quad \forall \boldsymbol{p} \in [\mathcal{P}(E)]^d$$

for extracting the polynomial part. These operators are required to satisfy the following orthogonality conditions:

$$\Pi_{\mathcal{R}}\boldsymbol{c} = \boldsymbol{0}, \quad \forall \boldsymbol{c} \in [\mathcal{C}(E)]^d \tag{24}$$

$$\Pi_{\mathcal{C}}\boldsymbol{r} = \boldsymbol{0}, \quad \forall \boldsymbol{r} \in [\mathcal{R}(E)]^d, \tag{25}$$

so that elements of $\mathcal{C}$ have no rigid body motions and elements of $\mathcal{R}$ have no constant strain modes, which means $\Pi_{\mathcal{C}}\Pi_{\mathcal{R}} = \Pi_{\mathcal{R}}\Pi_{\mathcal{C}} = \boldsymbol{0}$ and

$$\Pi_{\mathcal{P}} = \Pi_{\mathcal{R}} + \Pi_{\mathcal{C}}. \tag{26}$$

A properly defined projection map $\Pi_{\mathcal{C}}\boldsymbol{u}$ (i.e., it verifies (23) and (25)) will satisfy the following orthogonality property [30]:

$$a_E(\boldsymbol{u} - \Pi_{\mathcal{C}}\boldsymbol{u}, \boldsymbol{c}) = 0 \quad \forall \boldsymbol{c} \in [\mathcal{C}(E)]^d, \quad \boldsymbol{u} \in [\mathcal{W}(E)]^d, \tag{27}$$

which means that $\boldsymbol{u} - \Pi_{\mathcal{C}}\boldsymbol{u}$ is energetically orthogonal to $\mathcal{C}$; and since $\Pi_{\mathcal{R}}$ must satisfy (22) and (24), rigid body motions have zero strain energy and thus the energy orthogonality property extends to $\Pi_{\mathcal{P}}$:

$$a_E(\boldsymbol{u} - \Pi_{\mathcal{P}}\boldsymbol{u}, \boldsymbol{p}) = 0 \quad \forall \boldsymbol{p} \in [\mathcal{P}(E)]^d, \quad \boldsymbol{u} \in [\mathcal{W}(E)]^d. \tag{28}$$

So, any $\boldsymbol{u} \in \mathcal{W}(E)$ can be decomposed into three terms as follows:

$$\boldsymbol{u} = \Pi_{\mathcal{R}}\boldsymbol{u} + \Pi_{\mathcal{C}}\boldsymbol{u} + (\boldsymbol{u} - \Pi_{\mathcal{P}}\boldsymbol{u}), \tag{29}$$

that is, into a rigid body part, a constant strain part and the remaining nonpolynomial part. On substituting (29) into the bilinear form defined in (9), and relying on the properties (27) and (28) yields the bilinear form as [30]

$$a_E(\boldsymbol{u}, \boldsymbol{v}) = a_E(\Pi_{\mathcal{C}}\boldsymbol{u}, \Pi_{\mathcal{C}}\boldsymbol{v}) + a_E(\boldsymbol{u} - \Pi_{\mathcal{P}}\boldsymbol{u}, \boldsymbol{v} - \Pi_{\mathcal{P}}\boldsymbol{v}), \tag{30}$$

where the first term on the right-hand side is the bilinear form associated with the constant strain modes that provides consistency and the second term is the bilinear form associated with the nonpolynomial terms that provides stability.

The symmetric gradient tensor is given by

$$\boldsymbol{\varepsilon}(\boldsymbol{u}) = \frac{1}{2}\big(\boldsymbol{\nabla}\boldsymbol{u} + (\boldsymbol{\nabla}\boldsymbol{u})^{\mathrm{T}}\big)$$

and its volume average by

$$\hat{\boldsymbol{\varepsilon}}(\boldsymbol{u}) = \frac{1}{|E|}\int_E \varepsilon(\boldsymbol{u})d\boldsymbol{x} = \frac{1}{2|E|}\int_{\partial E} (\boldsymbol{u}\otimes\boldsymbol{n}_E + \boldsymbol{n}_E\otimes\boldsymbol{u})\, dS. \tag{31}$$

The skew-symmetric gradient tensor is given by

$$\boldsymbol{\omega}(\boldsymbol{u}) = \frac{1}{2}\big(\boldsymbol{\nabla}\boldsymbol{u} - (\boldsymbol{\nabla}\boldsymbol{u})^{\mathrm{T}}\big)$$

and its volume average is

$$\hat{\boldsymbol{\omega}}(\boldsymbol{u}) = \frac{1}{|E|}\int_E \boldsymbol{\omega}(\boldsymbol{u})d\boldsymbol{x} = \frac{1}{2|E|}\int_{\partial E} (\boldsymbol{u}\otimes\boldsymbol{n}_E - \boldsymbol{n}_E\otimes\boldsymbol{u})\, dS.$$

Let the basis for the space of rigid body motions be $[\boldsymbol{r}_\alpha]_{\alpha=1,\ldots,6}$, where $\boldsymbol{r}_1$, $\boldsymbol{r}_2$, $\boldsymbol{r}_3$ are rigid body

translation modes and $\boldsymbol{r}_4$, $\boldsymbol{r}_5$, $\boldsymbol{r}_6$ pure rotations modes about $\bar{\boldsymbol{x}}$ defined as [30]

$$\begin{aligned}
\boldsymbol{r}_1 &= [1 \quad 0 \quad 0]^{\mathrm{T}} & \boldsymbol{r}_4 &= [x_2 - \bar{x}_2 \quad \bar{x}_1 - x_1 \quad 0]^{\mathrm{T}} \\
\boldsymbol{r}_2 &= [0 \quad 1 \quad 0]^{\mathrm{T}} & \boldsymbol{r}_5 &= [\bar{x}_3 - x_3 \quad 0 \quad x_1 - \bar{x}_1]^{\mathrm{T}} \\
\boldsymbol{r}_3 &= [0 \quad 0 \quad 1]^{\mathrm{T}} & \boldsymbol{r}_6 &= [0 \quad x_3 - \bar{x}_3 \quad \bar{x}_2 - x_2]^{\mathrm{T}}.
\end{aligned}$$

A projection map to extract rigid body motions of $\boldsymbol{u}$ that verifies (22) and (24) is given by [30]

$$\Pi_{\mathcal{R}}\boldsymbol{u} = \bar{u}_1\boldsymbol{r}_1 + \bar{u}_2\boldsymbol{r}_2 + \bar{u}_3\boldsymbol{r}_3 + \hat{\omega}_{12}\boldsymbol{r}_4 + \hat{\omega}_{31}\boldsymbol{r}_5 + \hat{\omega}_{23}\boldsymbol{r}_6. \tag{32}$$

Let the basis for the space of constant strain modes be $[\boldsymbol{c}_\beta]_{\beta=1,\dots,6}$, where $\boldsymbol{c}_1$, $\boldsymbol{c}_2$, $\boldsymbol{c}_3$ are constant normal strains and $\boldsymbol{c}_4$, $\boldsymbol{c}_5$, $\boldsymbol{c}_6$ are constant shear strains, which are defined as [30]

$$\begin{aligned}
\boldsymbol{c}_1 &= [x_1 - \bar{x}_1 \quad 0 \quad 0]^{\mathrm{T}} & \boldsymbol{c}_4 &= [x_2 - \bar{x}_2 \quad x_1 - \bar{x}_1 \quad 0]^{\mathrm{T}} \\
\boldsymbol{c}_2 &= [0 \quad x_2 - \bar{x}_2 \quad 0]^{\mathrm{T}} & \boldsymbol{c}_5 &= [x_3 - \bar{x}_3 \quad 0 \quad x_1 - \bar{x}_1]^{\mathrm{T}} \\
\boldsymbol{c}_3 &= [0 \quad 0 \quad x_3 - \bar{x}_3]^{\mathrm{T}} & \boldsymbol{c}_6 &= [0 \quad x_3 - \bar{x}_3 \quad x_2 - \bar{x}_2]^{\mathrm{T}}.
\end{aligned}$$

A projection map to extract constant strain modes of $\boldsymbol{u}$ that verifies (23) and (25) is given by [30]

$$\Pi_{\mathcal{C}}\boldsymbol{u} = \hat{\varepsilon}_{11}\boldsymbol{c}_1 + \hat{\varepsilon}_{22}\boldsymbol{c}_2 + \hat{\varepsilon}_{33}\boldsymbol{c}_3 + \hat{\varepsilon}_{12}\boldsymbol{c}_4 + \hat{\varepsilon}_{31}\boldsymbol{c}_5 + \hat{\varepsilon}_{23}\boldsymbol{c}_6. \tag{33}$$

4.2.2. Stiffness matrix. To obtain the consistent and stable stiffness matrix, we start by discretizing with max-ent basis functions the following quantities on each integration cell:

$$\boldsymbol{u}^h(\boldsymbol{x}) = \sum_{a=1}^{m} \phi_a(\boldsymbol{x})\boldsymbol{u}_a \tag{34}$$

for the displacement field,

$$\boldsymbol{r}^h_\alpha(\boldsymbol{x}) = \sum_{a=1}^{m} = \phi_a(\boldsymbol{x})\boldsymbol{r}_\alpha(\boldsymbol{x}_a) \quad \alpha = 1, \dots, 6 \tag{35}$$

for the components of the basis for the space of rigid body motions, and

$$\boldsymbol{c}^h_\beta(\boldsymbol{x}) = \sum_{a=1}^{m} \phi_a(\boldsymbol{x})\boldsymbol{c}_\beta(\boldsymbol{x}_a) \quad \beta = 1, \dots, 6 \tag{36}$$

for the components of the basis for the space of constant strain modes. The discrete version of the projection map to extract the rigid body motions is obtained by substituting (34) and (35) into (32), which yields

$$\Pi_{\mathcal{R}}\boldsymbol{u}^h = \boldsymbol{N}\boldsymbol{P}_{\mathcal{R}}\boldsymbol{d},$$

where

$$\boldsymbol{N} = [(\boldsymbol{N})_1 \quad \cdots \quad (\boldsymbol{N})_a \quad \cdots \quad (\boldsymbol{N})_m]\ ;\ (\boldsymbol{N})_a = \begin{bmatrix} \phi_a & 0 & 0 \\ 0 & \phi_a & 0 \\ 0 & 0 & \phi_a \end{bmatrix},$$

$$\boldsymbol{d} = \begin{bmatrix} \boldsymbol{u}_1^{\mathrm{T}} & \cdots & \boldsymbol{u}_a^{\mathrm{T}} & \cdots & \boldsymbol{u}_m^{\mathrm{T}} \end{bmatrix}^{\mathrm{T}}\ ;\ \boldsymbol{u}_a = [u_{1a} \quad u_{2a} \quad u_{3a}]^{\mathrm{T}}$$

and

$$\boldsymbol{P}_{\mathcal{R}} = \boldsymbol{H}_{\mathcal{R}}\boldsymbol{W}_{\mathcal{R}}^{\mathrm{T}}$$

with

$$\boldsymbol{H}_{\mathcal{R}} = \begin{bmatrix} (\boldsymbol{H}_{\mathcal{R}})_1 \\ \vdots \\ (\boldsymbol{H}_{\mathcal{R}})_a \\ \vdots \\ (\boldsymbol{H}_{\mathcal{R}})_m \end{bmatrix},\quad (\boldsymbol{H}_{\mathcal{R}})_a = \begin{bmatrix} 1 & 0 & 0 \\ 0 & 1 & 0 \\ 0 & 0 & 1 \\ (x_{2a} - \bar{x}_2) & -(x_{1a} - \bar{x}_1) & 0 \\ -(x_{3a} - \bar{x}_3) & 0 & (x_{1a} - \bar{x}_1) \\ 0 & (x_{3a} - \bar{x}_3) & -(x_{2a} - \bar{x}_2) \end{bmatrix}^{\mathrm{T}}$$

and

$$\boldsymbol{W}_{\mathcal{R}} = \begin{bmatrix} (\boldsymbol{W}_{\mathcal{R}})_1 \\ \vdots \\ (\boldsymbol{W}_{\mathcal{R}})_a \\ \vdots \\ (\boldsymbol{W}_{\mathcal{R}})_m \end{bmatrix}, \quad (\boldsymbol{W}_{\mathcal{R}})_a = \begin{bmatrix} \bar{\phi}_a & 0 & 0 \\ 0 & \bar{\phi}_a & 0 \\ 0 & 0 & \bar{\phi}_a \\ q_{2a} & -q_{1a} & 0 \\ -q_{3a} & 0 & q_{1a} \\ 0 & q_{3a} & -q_{2a} \end{bmatrix}^{\mathrm{T}}, \quad q_{ia} = \frac{1}{2|E|} \int_{\partial E} \phi_a n_i^E \, dS.$$

Similarly, on substituting (34) and (36) into (33) leads to the following discrete version of the projection map to extract the constant strain modes:

$$\Pi_{\mathcal{C}} \boldsymbol{u}^h = \boldsymbol{N} \boldsymbol{P}_{\mathcal{C}} \boldsymbol{d},$$

where

$$\boldsymbol{P}_{\mathcal{C}} = \boldsymbol{H}_{\mathcal{C}} \boldsymbol{W}_{\mathcal{C}}^{\mathrm{T}}$$

with

$$\boldsymbol{H}_{\mathcal{C}} = \begin{bmatrix} (\boldsymbol{H}_{\mathcal{C}})_1 \\ \vdots \\ (\boldsymbol{H}_{\mathcal{C}})_a \\ \vdots \\ (\boldsymbol{H}_{\mathcal{C}})_m \end{bmatrix}, \quad (\boldsymbol{H}_{\mathcal{C}})_a = \begin{bmatrix} (x_{1a} - \bar{x}_1) & 0 & 0 \\ 0 & (x_{2a} - \bar{x}_2) & 0 \\ 0 & 0 & (x_{3a} - \bar{x}_3) \\ (x_{2a} - \bar{x}_2) & (x_{1a} - \bar{x}_1) & 0 \\ (x_{3a} - \bar{x}_3) & 0 & (x_{1a} - \bar{x}_1) \\ 0 & (x_{3a} - \bar{x}_3) & (x_{2a} - \bar{x}_2) \end{bmatrix}^{\mathrm{T}}$$

and

$$\boldsymbol{W}_{\mathcal{C}} = \begin{bmatrix} (\boldsymbol{W}_{\mathcal{C}})_1 \\ \vdots \\ (\boldsymbol{W}_{\mathcal{C}})_a \\ \vdots \\ (\boldsymbol{W}_{\mathcal{C}})_m \end{bmatrix}, \; (\boldsymbol{W}_{\mathcal{C}})_a = \begin{bmatrix} 2q_{1a} & 0 & 0 \\ 0 & 2q_{2a} & 0 \\ 0 & 0 & 2q_{3a} \\ q_{2a} & q_{1a} & 0 \\ q_{3a} & 0 & q_{1a} \\ 0 & q_{3a} & q_{2a} \end{bmatrix}^{\mathrm{T}}, \; q_{ia} = \frac{1}{2|E|} \int_{\partial E} \phi_a n_i^E \, dS.$$

By virtue of (26), $\boldsymbol{\Pi}_{\mathcal{P}} \boldsymbol{u}^h = \boldsymbol{\Pi}_{\mathcal{R}} \boldsymbol{u}^h + \boldsymbol{\Pi}_{\mathcal{C}} \boldsymbol{u}^h$ and $\boldsymbol{P}_{\mathcal{P}} = \boldsymbol{P}_{\mathcal{R}} + \boldsymbol{P}_{\mathcal{C}}$. For the linear elastostatic boundary-value problem, the discrete version of the bilinear form is given by the virtual element decomposition on each cell (see (30)) as follows:

$$\begin{aligned} a_E(\boldsymbol{u}^h, \boldsymbol{u}^h) &= a_E(\boldsymbol{\Pi}_{\mathcal{C}} \boldsymbol{u}^h, \boldsymbol{\Pi}_{\mathcal{C}} \boldsymbol{v}^h) + a_E(\boldsymbol{u}^h - \boldsymbol{\Pi}_{\mathcal{P}} \boldsymbol{u}^h, \boldsymbol{v}^h - \boldsymbol{\Pi}_{\mathcal{P}} \boldsymbol{v}^h) \\ &= \boldsymbol{v}^{\mathrm{T}} \boldsymbol{W}_{\mathcal{C}} \boldsymbol{H}_{\mathcal{C}}^{\mathrm{T}} \, a_E(\boldsymbol{N}^{\mathrm{T}}, \boldsymbol{N}) \, \boldsymbol{H}_{\mathcal{C}} \boldsymbol{W}_{\mathcal{C}}^{\mathrm{T}} \boldsymbol{d} + \boldsymbol{v}^{\mathrm{T}} (\boldsymbol{I}_{3m} - \boldsymbol{P}_{\mathcal{P}})^{\mathrm{T}} \, a_E(\boldsymbol{N}^{\mathrm{T}}, \boldsymbol{N}) \, (\boldsymbol{I}_{3m} - \boldsymbol{P}_{\mathcal{P}}) \boldsymbol{d} \\ &= \boldsymbol{v}^{\mathrm{T}} \boldsymbol{W}_{\mathcal{C}} \boldsymbol{H}_{\mathcal{C}}^{\mathrm{T}} \boldsymbol{K} \boldsymbol{H}_{\mathcal{C}} \boldsymbol{W}_{\mathcal{C}}^{\mathrm{T}} \boldsymbol{d} + \boldsymbol{v}^{\mathrm{T}} (\boldsymbol{I}_{3m} - \boldsymbol{P}_{\mathcal{P}})^{\mathrm{T}} \boldsymbol{K} (\boldsymbol{I}_{3m} - \boldsymbol{P}_{\mathcal{P}}) \boldsymbol{d}, \end{aligned} \tag{37}$$

where $\boldsymbol{I}_{3m}$ is the identity $(3m \times 3m)$ matrix, with m being the number of nodes that contribute in the cell, $\boldsymbol{K}$ is the exact stiffness matrix, and $\boldsymbol{v}$ is a vector of arbitrary nodal coefficients that is associated with the displacement test functions.

Regarding the first term on the right-hand side of the last equality in (37), in Reference [30] it was shown that $\boldsymbol{H}_{\mathcal{C}}^{\mathrm{T}} \boldsymbol{K} \boldsymbol{H}_{\mathcal{C}} = |E| \boldsymbol{D}$, where $\boldsymbol{D}$ is the constitutive matrix for an isotropic linear elastic material; and regarding the second term, the exact stiffness can conveniently be replaced by an approximate stiffness denoted by $\boldsymbol{S}$. Thus, the final expression for the stiffness matrix associated with the integration cell can be written as:

$$\boldsymbol{K}_E = |E| \boldsymbol{W}_{\mathcal{C}} \boldsymbol{D} \boldsymbol{W}_{\mathcal{C}}^{\mathrm{T}} + (\boldsymbol{I}_{3m} - \boldsymbol{P}_{\mathcal{P}})^{\mathrm{T}} \boldsymbol{S} (\boldsymbol{I}_{3m} - \boldsymbol{P}_{\mathcal{P}}),$$

Prepared using nmeauth.cls

where

$$\boldsymbol{D} = \frac{E}{(1+\nu)(1-2\nu)} \begin{bmatrix} 1-\nu & \nu & \nu & 0 & 0 & 0 \\ \nu & 1-\nu & \nu & 0 & 0 & 0 \\ \nu & \nu & 1-\nu & 0 & 0 & 0 \\ 0 & 0 & 0 & 2(1-2\nu) & 0 & 0 \\ 0 & 0 & 0 & 0 & 2(1-2\nu) & 0 \\ 0 & 0 & 0 & 0 & 0 & 2(1-2\nu) \end{bmatrix},$$

where E is the Young's modulus and ν is the Poisson's ratio.

With respect to the stability stiffness, any choice for $\boldsymbol{S}$ that leads to a stability stiffness that is symmetric positive definite and scales like the exact bilinear form $a(\cdot,\cdot)$ is sufficient [3]. Herein we adopt $\boldsymbol{S}$ given as [32]

$$\boldsymbol{S} = \alpha \left(\boldsymbol{I}_{3m} - \boldsymbol{H}_{\mathcal{P}} \left(\boldsymbol{H}_{\mathcal{P}}^{\mathrm{T}} \boldsymbol{H}_{\mathcal{P}} \right)^{-1} \boldsymbol{H}_{\mathcal{P}}^{\mathrm{T}} \right) = \alpha \boldsymbol{M}, \tag{39}$$

where $\boldsymbol{H}_{\mathcal{P}} = \boldsymbol{H}_{\mathcal{R}} + \boldsymbol{H}_{\mathcal{C}}$ and $\alpha = \alpha^* \operatorname{trace}\left(|E| \boldsymbol{W}_{\mathcal{C}} \boldsymbol{D} \boldsymbol{W}_{\mathcal{C}}^{\mathrm{T}} \right)$ is the scaling parameter. In this approach, α^* is a positive constant and is usually chosen by studying its influence on the H^1 seminorm (see References [29, 30]).

5. PATCH TEST SATISFACTION

In this section, it is shown that the patch test is satisfied for the proposed formulation. To this end, we choose the linear elastostatic problem and impose the linear field $\boldsymbol{u}(\boldsymbol{x}) = \boldsymbol{p}(\boldsymbol{x}) \in [\mathcal{P}(E)]^d$ on the entire boundary. Hence, the exact solution for the patch test must be $\boldsymbol{u}(\boldsymbol{x}) = \boldsymbol{p}(\boldsymbol{x})$. Since $\boldsymbol{p} - \Pi_{\mathcal{P}} \boldsymbol{p} = 0$, then from (30) and from the definition of $a(\boldsymbol{u}, \boldsymbol{v})$ in (9), we obtain

$$a_E(\boldsymbol{p}, \boldsymbol{v}) = \int_E \boldsymbol{\sigma}(\Pi_{\mathcal{C}} \boldsymbol{p}) : \boldsymbol{\varepsilon}(\Pi_{\mathcal{C}} \boldsymbol{v}) \, d\boldsymbol{x}. \tag{40}$$

We also note that $\boldsymbol{\varepsilon}(\Pi_{\mathcal{P}} \boldsymbol{p}) = \boldsymbol{\varepsilon}(\Pi_{\mathcal{R}} \boldsymbol{p}) + \boldsymbol{\varepsilon}(\Pi_{\mathcal{C}} \boldsymbol{p}) = \boldsymbol{\varepsilon}(\Pi_{\mathcal{C}} \boldsymbol{p}) = \boldsymbol{\varepsilon}(\boldsymbol{p})$, where $\Pi_{\mathcal{P}} \boldsymbol{p} = \boldsymbol{p}$ and the fact that rigid body motions $\Pi_{\mathcal{R}} \boldsymbol{p}$ have zero strains have been used. In addition, $\boldsymbol{\sigma}(\Pi_{\mathcal{C}} \boldsymbol{p}) = \mathcal{D} : \boldsymbol{\varepsilon}(\Pi_{\mathcal{C}} \boldsymbol{p})$,

where $\mathcal{D}$ is the elastic modulus tensor, and using the preceding result, (40) can be rewritten as

$$a_E(\boldsymbol{p},\boldsymbol{v}) = \int_E \boldsymbol{\sigma}(\boldsymbol{p}) : \boldsymbol{\varepsilon}(\Pi_{\mathcal{C}}\boldsymbol{v})\, d\boldsymbol{x}. \tag{41}$$

Now, since $\boldsymbol{u}(\boldsymbol{x}) = \boldsymbol{p}(\boldsymbol{x}) \in [\mathcal{P}(E)]^d$ is the exact solution, $\boldsymbol{\sigma}(\boldsymbol{p})$ is a constant. Let $\boldsymbol{\sigma}^c$ denote the constant stress field and observe that the strain associated with $\Pi_{\mathcal{C}}\boldsymbol{v}$ is the volume average of the strain, i.e., $\boldsymbol{\varepsilon}(\Pi_{\mathcal{C}}\boldsymbol{v}) = \hat{\boldsymbol{\varepsilon}}(\boldsymbol{v})$. Thus, from (41) we get

$$a_E(\boldsymbol{p},\boldsymbol{v}) = \boldsymbol{\sigma}^c : \int_E \hat{\boldsymbol{\varepsilon}}(\boldsymbol{v})\, d\boldsymbol{x} = \boldsymbol{\sigma}^c : \frac{1}{2|E|}\int_{\partial E} (\boldsymbol{v}\otimes\boldsymbol{n}_E + \boldsymbol{n}_E\otimes\boldsymbol{v})\, dS. \tag{42}$$

The final step is to substitute the nodal approximation $\boldsymbol{v}^h(\boldsymbol{x}) = \phi_a(\boldsymbol{x})\boldsymbol{v}_a$ into (42). We also use the symmetry of the stress tensor and sum over all the cells to get

$$\sum_E a_E(\boldsymbol{p},\boldsymbol{v}^h) = \sum_E \left(\frac{1}{|E|}\int_{\partial E} \hat{\boldsymbol{B}}_a^{\mathrm{T}}\boldsymbol{\sigma}^c\, dS\right)\boldsymbol{v}_a = \boldsymbol{f}_a\cdot\boldsymbol{v}_a,$$

where

$$\hat{\boldsymbol{B}}_a = \begin{bmatrix} \phi_a n_1^E & 0 & 0 \\ 0 & \phi_a n_2^E & 0 \\ 0 & 0 & \phi_a n_3^E \\ \phi_a n_2^E & \phi_a n_1^E & 0 \\ \phi_a n_3^E & 0 & \phi_a n_1^E \\ 0 & \phi_a n_3^E & \phi_a n_2^E \end{bmatrix}$$

and $\boldsymbol{f}_a$ is an interior nodal force. Since the patch test produces a state of constant strains (and stresses), all the interior nodal forces must be identically equal to zero. Therefore, for the patch test to be satisfied it suffices to show that

$$\boldsymbol{f}_a = \sum_E \frac{1}{|E|}\int_{\partial E} \hat{\boldsymbol{B}}_a^{\mathrm{T}}\boldsymbol{\sigma}^c\, dS = \boldsymbol{0}, \tag{43}$$

where the assembly is over all the cells that have a non-zero intersection with the support of ϕ_a. To compute (43), we choose Gauss integration over the faces of the integration cells, and since the

evaluation of $\hat{\boldsymbol{B}}_a$ at a given interior face will arise from two adjacent cells in the assembly, the two contributions cancel each other. Thus, the net contribution to $\boldsymbol{f}_a$ from all the interior faces vanishes, and hence (43) is satisfied.

6. NUMERICAL EXAMPLES

Numerical examples are presented to demonstrate the consistency and stability of the maximum-entropy meshfree method using the virtual element decomposition. We adopt the acronym MEM-VED to refer to this method in the remainder of this section. In the computations, the following quadrature rules are used for numerical integration over a background mesh of three-node triangular and four-node tetrahedral cells: 1-point Gauss rule on each face of the cell (surface Gauss point) to compute the surface integrals that appear in the consistency and stability stiffness matrices, and in the stability stiffness of the Poisson problem an additional 1-point Gauss rule within each cell (volume Gauss point). Note that at the surface Gauss points only basis functions are computed — derivatives are not needed.

In the standard maximum-entropy meshfree method (MEM), the stiffness matrix contains the usual volume integral and hence it is numerically integrated using standard Gauss integration within each cell. The same background mesh is adopted for the MEM and MEM-VED approaches.

6.1. Poisson problem

6.1.1. Patch test. The boundary-value problem (4) is solved with $f(\boldsymbol{x}) = 0$ and $g(\boldsymbol{x}) = 1+2x+3y$ within a unit square. The background meshes used in the study are shown in Figure 2. Numerical results for the relative error in the L^2 norm and the H^1 seminorm are presented in Tables I and II, respectively. The basis function support parameter is set to $\gamma = 2.0$ in the Gaussian prior weight

function. For the standard Gauss integration, several choices for the number of volume Gauss points are tested. Numerical results confirm that the patch test is met to machine precision only for the MEM-VED scheme.

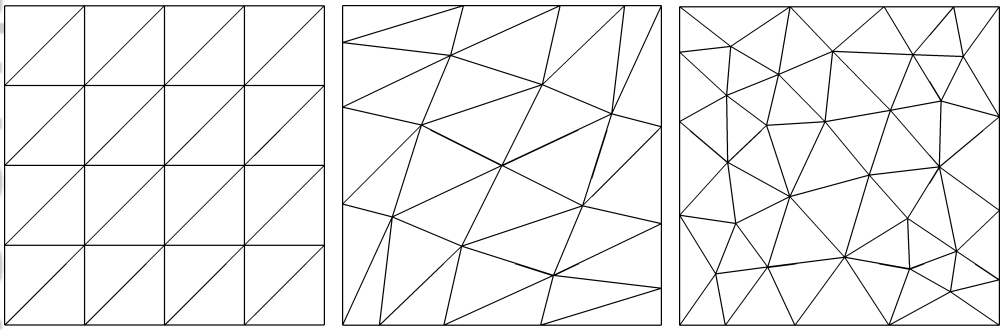

(a) (b) (c)

Figure 2: Background meshes used for the patch test on the Poisson problem. (a) Regular mesh, (b) distorted mesh, and (c) unstructured mesh.

Table I: Relative error in the L^2 norm for the patch tests on the Poisson problem.

Method	Gauss rule	Regular	Distorted	Unstructured
MEM	1-point	1.5×10^{-4}	1.0×10^{-2}	1.1×10^{-2}
MEM	3-point	8.1×10^{-5}	9.8×10^{-4}	1.4×10^{-3}
MEM	6-point	6.4×10^{-5}	6.9×10^{-4}	1.0×10^{-3}
MEM	12-point	1.7×10^{-5}	1.9×10^{-4}	2.5×10^{-4}
MEM–VED	1-pt/1-pt	3.0×10^{-15}	3.7×10^{-15}	7.6×10^{-15}

Table II: Relative error in the H^1 seminorm for the patch tests on the Poisson problem.

Method	Gauss rule	Regular	Distorted	Unstructured
MEM	1-point	1.5×10^{-3}	1.3×10^{-1}	2.0×10^{-1}
MEM	3-point	6.8×10^{-4}	1.3×10^{-2}	3.1×10^{-2}
MEM	6-point	6.6×10^{-4}	8.8×10^{-3}	2.3×10^{-2}
MEM	12-point	1.2×10^{-4}	2.2×10^{-3}	5.7×10^{-3}
MEM–VED	1-pt/1-pt	1.6×10^{-13}	1.2×10^{-13}	2.3×10^{-13}

6.1.2. Convergence. The convergence rates in the L^2 norm and H^1 seminorm are studied for the two-dimensional Poisson problem (4). The unstructured meshes shown in Figure 3 are considered for the convergence tests. In the Poisson problem, $f(\boldsymbol{x})$ is chosen in accordance with the exact solution $u(\boldsymbol{x}) = 16xy(1-x)(1-y)$. The Dirichlet boundary condition $g(\boldsymbol{x}) = 0$ is imposed on the entire boundary of the domain.

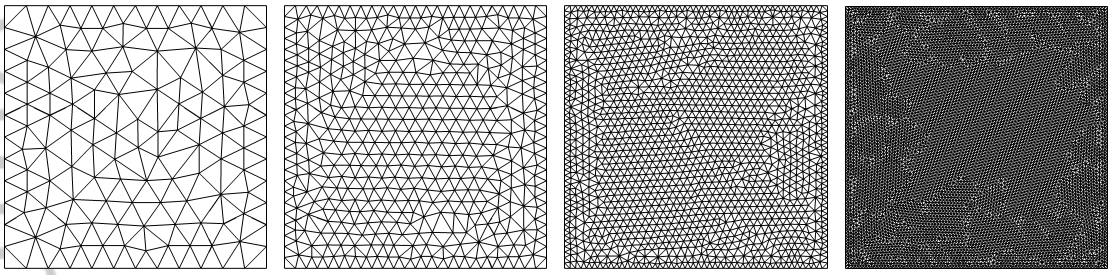

(a) (b) (c) (d)

Figure 3: Sequence of background meshes used for the convergence study on the Poisson problem.

As a first test, we compare the convergence rates that are delivered by the MEM using various standard Gauss integration rules and the MEM-VED approach. The support parameter of the maxent basis functions is set to $\gamma = 2.0$. The optimal rates of convergence are 2 and 1 in the L^2 norm and the H^1 seminorm, respectively. Figure 4 depicts the convergence rates for both the MEM and the MEM-VED approaches, and the reference rates for the classical three-node FE triangle. It is observed that the optimal rate of convergence is delivered by the MEM-VED approach in the L^2 norm, and in the H^1 seminorm the convergence rate is higher than the optimal rate of 1, which is, however, not surprising since this rate in meshfree methods can be improved because the support of the meshfree basis function is larger than its finite element counterpart.

For the MEM method, the convergence rate in the L^2 norm is suboptimal for 1-point Gauss rule, and with 3-point rule the accuracy is improved and the convergence rate becomes optimal. On the other hand, the convergence rate in the H^1 seminorm is suboptimal for 1- to 6-point Gauss rules; a 12-point Gauss rule is needed to recover the optimal rate with accuracy that is comparable to the MEM-VED approach. It is also evident from these plots that the accuracy of the MEM-VED approach is superior to the accuracy of the classical three-node FE triangle.

The effect of the support size of the nodal basis function on the convergence rates is investigated. Three values for γ are considered. The resulting rates of convergence are provided in Figure 5, where it is observed that optimal convergence rates (L^2 and H^1) are delivered by the MEM-VED scheme for all three values of γ.

6.2. Linear elastostatics

6.2.1. Two-dimensional patch test. We solve the boundary-value problem (8) with $\boldsymbol{b} = \boldsymbol{0}$ and $\boldsymbol{g} = \{x_1 \quad x_1 + x_2\}^{\mathrm{T}}$ prescribed along the entire boundary. Plane strain condition is assumed with

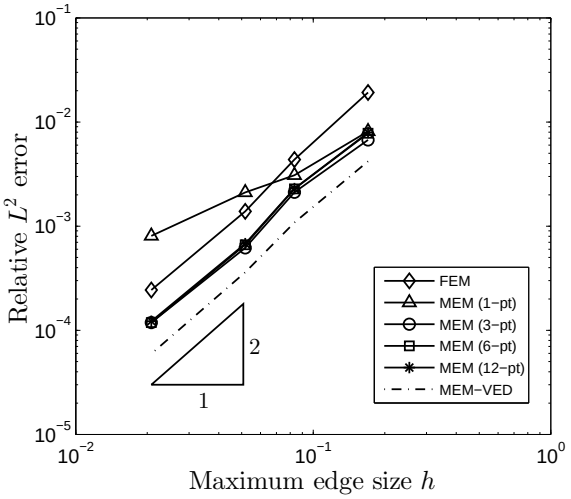

(a)

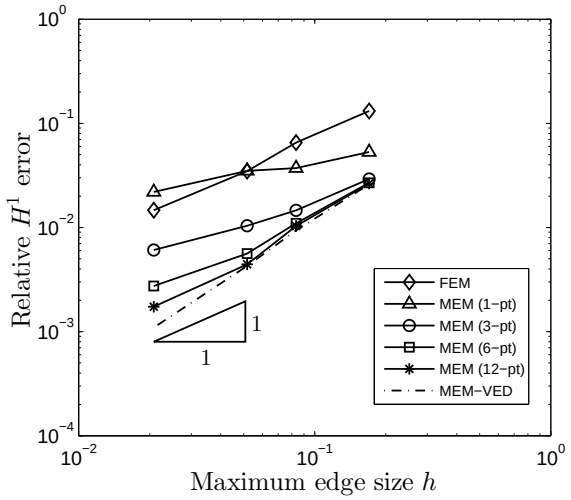

(b)

Figure 4: Rates of convergence for the Poisson problem. (a) L^2 norm and (b) H^1 seminorm. Optimal rates of 2 and 1 in the L^2 norm and the H^1 seminorm, respectively, are delivered by the MEM-VED approach. For the MEM approach to exhibit optimal rates with accuracy that is comparable to the MEM-VED approach, 3-point Gauss rule (L^2 norm) and 12-point Gauss rule (H^1 seminorm) are needed.

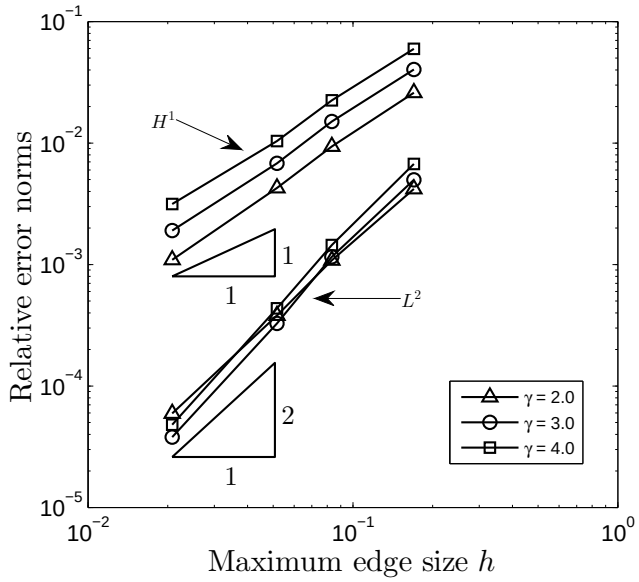

Figure 5: Rates of convergence of the MEM-VED scheme for the Poisson problem. Three values for the support parameter γ are chosen in the Gaussian prior weight function. For all cases, the MEM-VED method delivers optimal convergence rates in the L^2 norm and the H^1 seminorm.

the following material parameters: $E = 1 \times 10^7$ and $\nu = 0.3$. The background meshes used in this study are the same meshes that were used in the patch test for the Poisson problem (see Figure 2). The basis function support parameter is set to $\gamma = 2.0$ in the Gaussian prior weight function. Numerical results for the relative error in the L^2 norm and the H^1 seminorm are presented in Tables III and IV, respectively. For Gauss integration, several choices for the number of volume Gauss points are tested. Numerical results confirm that the patch test is met to machine precision only for the MEM-VED scheme.

6.2.2. Three-dimensional patch test. The boundary-value problem (8) is solved with $\boldsymbol{b} = \boldsymbol{0}$ and $\boldsymbol{g} = \{x_1 \quad x_1 + x_2 \quad x_1 + x_2 + x_3\}^{\mathrm{T}}$ applied along the entire boundary. The material parameters

Table III: Relative error in the L^2 norm for the two-dimensional elastostatic patch tests.

Method	Gauss rule	Regular	Distorted	Unstructured
MEM	1-point	4.7×10^{-4}	3.0×10^{-2}	2.6×10^{-2}
MEM	3-point	1.8×10^{-4}	2.8×10^{-3}	3.8×10^{-3}
MEM	6-point	1.9×10^{-4}	1.2×10^{-3}	1.4×10^{-3}
MEM	12-point	3.2×10^{-5}	5.8×10^{-4}	7.2×10^{-4}
MEM–VED	1-pt/1-pt	8.7×10^{-15}	1.7×10^{-13}	2.5×10^{-13}

Table IV: Relative error in the H^1 seminorm for the two-dimensional elastostatic patch tests.

Method	Gauss rule	Regular	Distorted	Unstructured
MEM	1-point	2.2×10^{-3}	2.1×10^{-1}	2.7×10^{-1}
MEM	3-point	9.7×10^{-4}	1.9×10^{-2}	4.2×10^{-2}
MEM	6-point	8.4×10^{-4}	6.5×10^{-3}	1.5×10^{-2}
MEM	12-point	1.5×10^{-4}	3.4×10^{-3}	7.7×10^{-3}
MEM–VED	1-pt/1-pt	9.2×10^{-14}	5.2×10^{-13}	1.0×10^{-12}

are set to $E = 1 \times 10^7$ and $\nu = 0.3$. The background meshes considered in this study are shown in Figure 6. The basis function support parameter is set to $\gamma = 2.0$ in the Gaussian prior weight function. The relative error in the L^2 norm and the H^1 seminorm for the numerical solution are

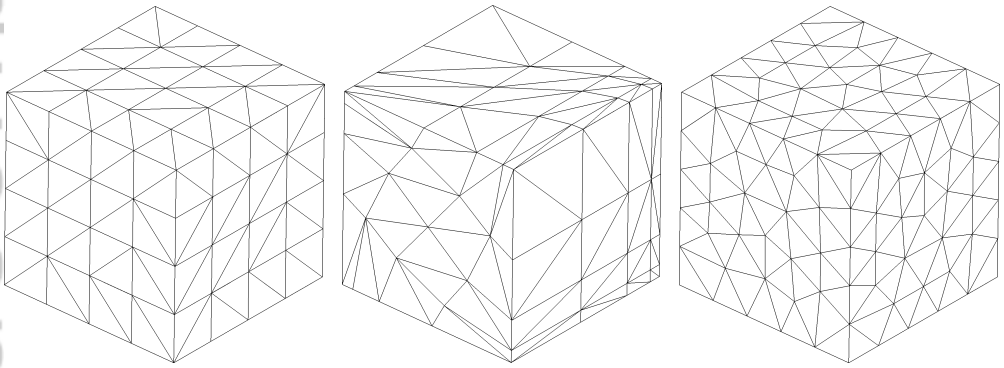

(a) (b) (c)

Figure 6: Background meshes used for the three-dimensional patch test on the linear elastostatic boundary-value problem. (a) Regular mesh, (b) distorted mesh, and (c) unstructured mesh.

presented in Tables V and VI, respectively. For Gauss integration, several choices for the number of volume Gauss points are tested. Numerical results confirm that the patch test is met to machine precision only for the MEM-VED scheme.

6.2.3. Cantilever beam. The convergence upon mesh refinement is studied on a cantilever beam of unit thickness subjected to a parabolic end load P. Figure 7 presents the geometry and boundary conditions. The sequence of unstructured meshes used in the study are shown in Figure 8. Plane strain condition is assumed. The essential boundary conditions on the clamped edge are applied

Table V: Relative error in the L^2 norm for the three-dimensional elastostatic patch tests.

Method	Gauss rule	Regular	Distorted	Unstructured
MEM	1-point	6.5×10^{-3}	3.6×10^{-2}	5.5×10^{-2}
MEM	4-point	8.4×10^{-4}	6.6×10^{-3}	1.5×10^{-2}
MEM	10-point	1.1×10^{-4}	2.4×10^{-3}	5.7×10^{-3}
MEM	24-point	1.6×10^{-3}	2.7×10^{-3}	2.8×10^{-3}
MEM–VED	1-pt/1-pt	1.0×10^{-13}	1.4×10^{-13}	1.6×10^{-12}

Table VI: Relative error in the H^1 seminorm for the three-dimensional elastostatic patch tests.

Method	Gauss rule	Regular	Distorted	Unstructured
MEM	1-point	3.9×10^{-2}	3.8×10^{-1}	7.1×10^{-1}
MEM	4-point	5.4×10^{-3}	7.6×10^{-2}	2.3×10^{-1}
MEM	10-point	6.6×10^{-4}	2.6×10^{-2}	8.8×10^{-2}
MEM	24-point	1.2×10^{-2}	2.6×10^{-2}	4.9×10^{-2}
MEM–VED	1-pt/1-pt	4.5×10^{-13}	6.1×10^{-13}	7.7×10^{-12}

according to the analytical solution given by Timoshenko and Goodier [33]:

$$u_x = -\frac{Py}{6\bar{E}I}\left((6L-3x)x + (2+\bar{\nu})y^2 - \frac{3D^2}{2}(1+\bar{\nu})\right),$$
$$u_y = \frac{P}{6\bar{E}I}\left(3\bar{\nu}y^2(L-x) + (3L-x)x^2\right),$$

where $\bar{E} = E/\left(1-\nu^2\right)$ with the Young's modulus set to $E = 10^7$ psi and $\bar{\nu} = \nu/\left(1-\nu\right)$ with the Poisson's ratio set to $\nu = 0.3$; $L = 8$ in. is the length of the beam, $D = 4$ in. is the height of the beam, and I is the second-area moment of the beam section. The total load on the traction boundary is $P = -1000$ lbf.

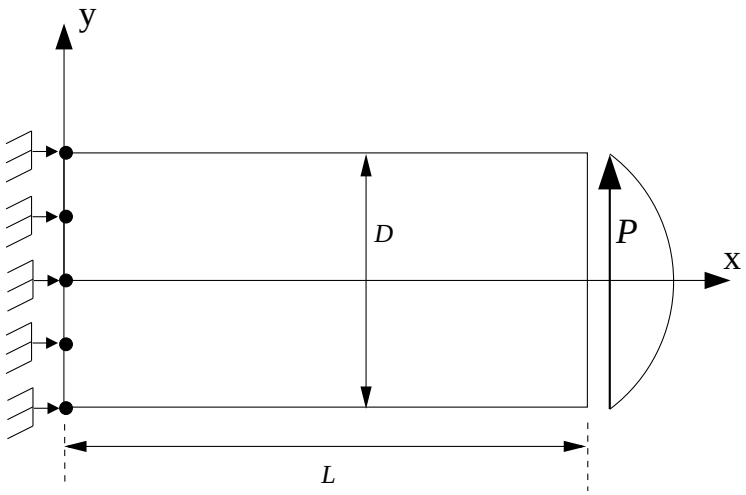

Figure 7: Model geometry and boundary conditions for the cantilever beam problem.

In order to set the scaling parameter in the stability stiffness, a sensitivity analysis of α^* in the H^1 seminorm is performed over the background mesh shown in Figure 8(c). The basis function support parameter is set to $\gamma = 2.0$ in the Gaussian prior weight function. The sensitivity analysis is shown in Figure 9, where a minimum is attained at around $\alpha^* = 10^{-4}$. Smaller values for α^* give almost the same error. The reference error value for the three-node FE triangle is also shown in the plot. $\alpha^* = 10^{-4}$ is adopted in the remainder of this example.

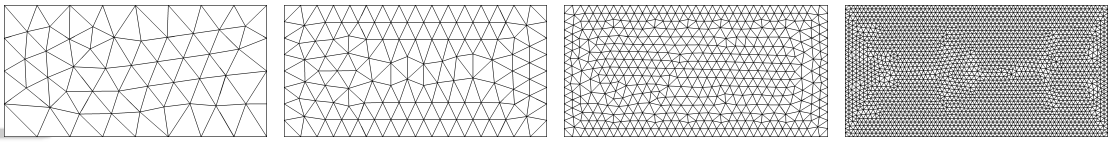

(a) (b) (c) (d)

Figure 8: Sequence of background meshes used for the convergence study on the cantilever beam problem.

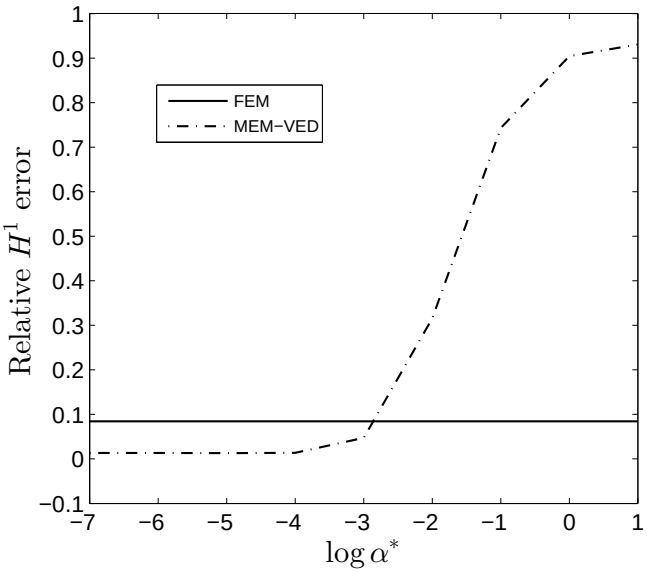

Figure 9: Cantilever beam problem. Sensitivity analysis of α^* in the H^1 seminorm.

The next study is devoted to comparing the convergence rates that are delivered by the MEM using various standard Gauss integration rules and the MEM-VED approach upon mesh refinement. Results for the three-node FE triangle are also shown for reference purposes. Convergence plots are shown in Figure 10. From Figure 10(a), we observe that the L^2 rate using the MEM-VED scheme is optimal, whereas the MEM needs a 3-point Gauss rule to deliver the optimal rate with comparable

accuracy. The convergence rates in the H^1 seminorm are shown in Figure 10(b), where it is observed that the MEM-VED approach delivers a convergence rate that is higher than the optimal rate of 1, which is, however, not surprising since the convergence rate in meshfree methods can be affected by the support size of the basis functions. The support size is controlled by the parameter γ, which in this example was set to 2.0. On the other hand, the convergence for the MEM behaves erratically for 1- and 3-point Gauss rule with poor accuracy; a 6-point Gauss rule is needed to recover the optimal rate with an accuracy comparable to MEM-VED approach. It is also evident from these plots that the accuracy of the MEM-VED method is superior to the accuracy of the classical three-node FE triangle.

A final study is performed to investigate the effect of the support size of the nodal basis function. Three values are considered for γ. The resulting rates of convergence are provided in Figure 11, where it is observed that the convergence rates in the L^2 norm and H^1 seminorm are optimal for all three values of γ.

6.2.4. Pressurized thick-walled cylinder. Rates of convergence are studied for the problem of a pressurized thick-walled cylinder. Figure 12 depicts the geometry and boundary conditions. The sequence of unstructured meshes used in the study are shown in Figure 13. The cylinder is assumed to be sufficiently long so that plain strain conditions are valid. The exact solution to this problem is obtained from the analytical solution in the radial direction and is given by [34]

$$u_r = \frac{(1+\nu)r_i^2 p}{E(r_o^2 - r_i^2)} \left(\frac{r_o^2}{r} + r(1-2\nu) \right),$$

where $r_i \leq r \leq r_o$ is the radius of thick-walled cylinder with $r_i = 3$ in. and $r_o = 9$ in; the Young's modulus is set to $E = 1000$ psi and the Poisson's ratio to $\nu = 0.3$. The internal pressure is set to $p = 1$ psi.

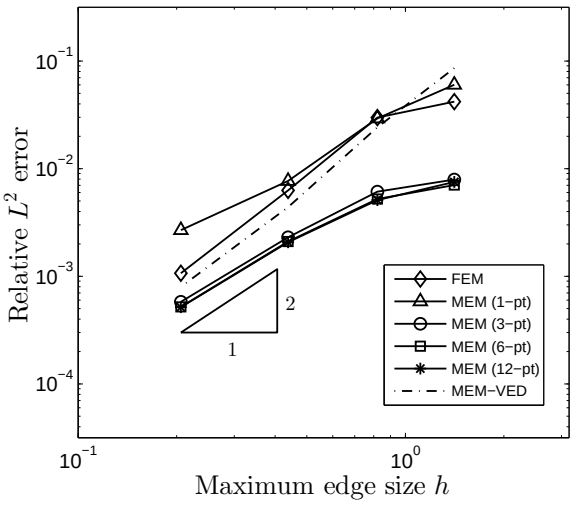

(a)

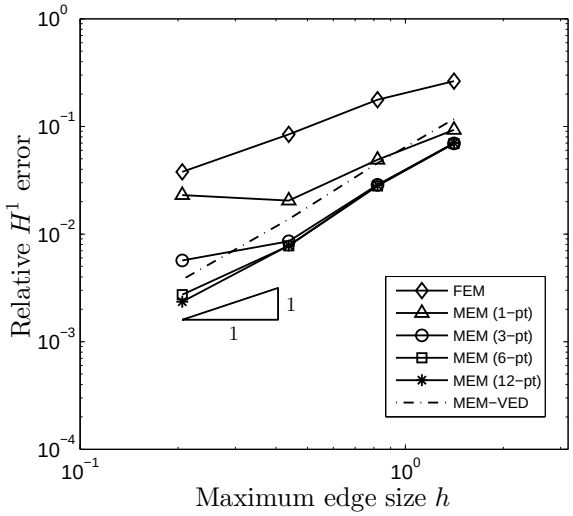

(b)

Figure 10: Rates of convergence for the cantilever beam problem. Optimal rates of 2 and 1 in the L^2 norm and the H^1 seminorm, respectively, are delivered by the MEM-VED approach. The convergence in the H^1 seminorm behaves erratically for the MEM method using 1- and 3-point Gauss rules due to integration errors; a 6-point Gauss rule is needed to recover the optimal rate.

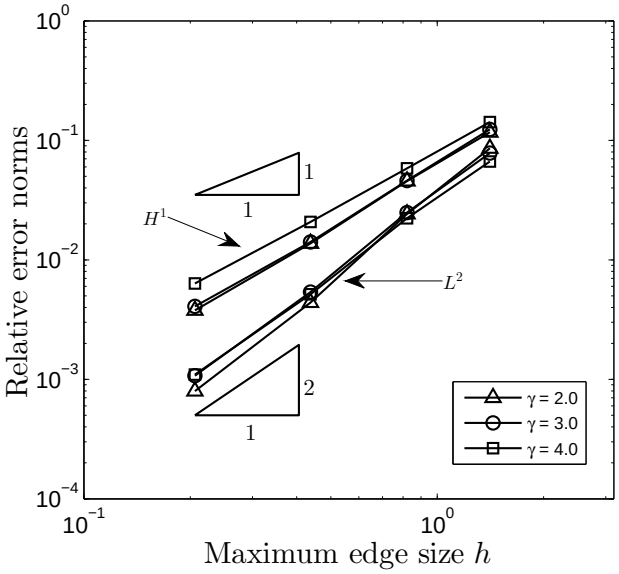

Figure 11: Rates of convergence for the cantilever beam problem using the MEM-VED scheme. Three values for the support parameter γ are chosen in the Gaussian prior weight function. Optimal convergence rates in the L^2 norm and the H^1 seminorm are obtained for all three cases.

To set the scaling parameter in the stability stiffness, a sensitivity analysis of α^* in the H^1 seminorm is performed over the background mesh shown in Figure 13(d). The basis function support parameter is set to $\gamma = 2.0$ in the Gaussian prior weight function. The sensitivity analysis is shown in Figure 14, where a minimum is attained at around $\alpha^* = 10^{-4}$. Smaller values for α^* give almost the same error. The reference error value for the three-node FE triangle is also shown in the plot. $\alpha^* = 10^{-4}$ is adopted in the remainder of this example.

We compare the convergence rates that are delivered by the MEM for various standard Gauss integration rules and the MEM-VED approach. Results for the three-node FE triangle are also included for reference purposes. The basis function support parameter is set to $\gamma = 2.0$ in the Gaussian prior weight function. Figure 15 presents the convergence rates for the MEM and the

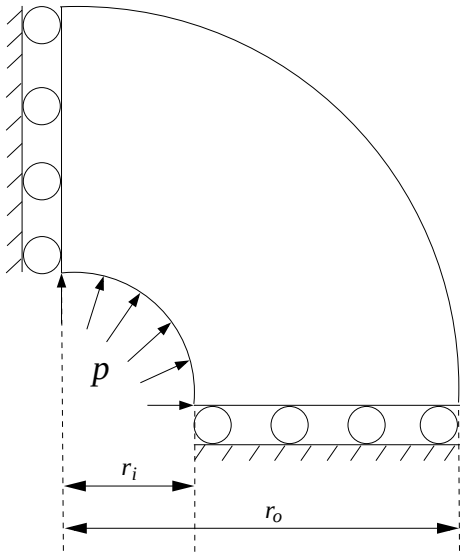

Figure 12: Model geometry and boundary conditions for the pressurized thick-walled cylinder problem.

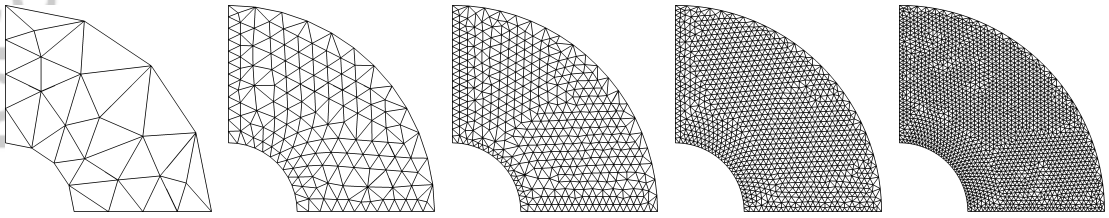

Figure 13: Sequence of background meshes used for the convergence study on the pressurized thick-walled cylinder problem.

MEM-VED approaches, and the three-node FE triangle. It is observed that the optimal rates of convergence are delivered by the MEM-VED approach in both the L^2 norm and the H^1 seminorm. On the other hand, for the MEM approach, the convergence in the H^1 seminorm is erratic for 1- and 3-point Gauss rules, and 6-point rule is needed to recover the optimal convergence rate. A

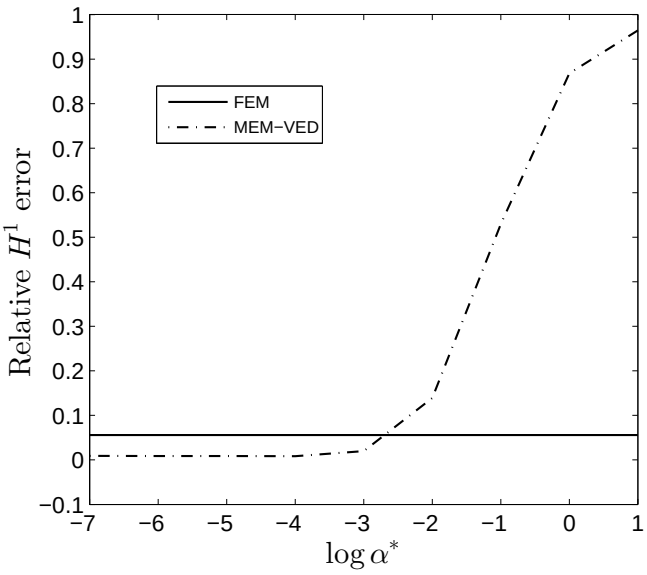

Figure 14: Pressurized thick-walled cylinder problem. Sensitivity analysis of α^* in the H^1 seminorm.

similar trend is observed for the L^2 norm. It is also evident that the MEM approach with 1-point and 3-point rules is less accurate than the MEM-VED scheme. The superior accuracy exhibited by the MEM-VED approach over the classical three-node FE triangle is also evident in these plots.

A study to investigate the effect of the support size of the nodal basis function is conducted. Three values are considered for γ. The rates of convergence are provided in Figure 16, where it is observed that the optimal rates of convergence are delivered by the MEM-VED scheme in both the L^2 norm and the H^1 seminorm for the three values of γ.

6.2.5. Infinite elastic stratum. As the last example, we consider the problem of an infinite elastic stratum subjected to a uniform pressure on the top surface as shown in Figure 17. In addition, the gravitational field of magnitude $g = 9.8$ m/s^2 acts over the stratum. The height of the stratum is $h = 1$ m and the uniform pressure is $q = 10^6$ Pa. Given the infinite length along the x and z

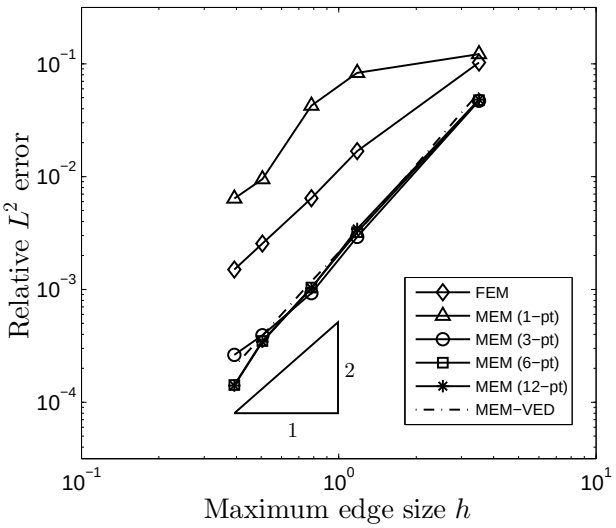

(a)

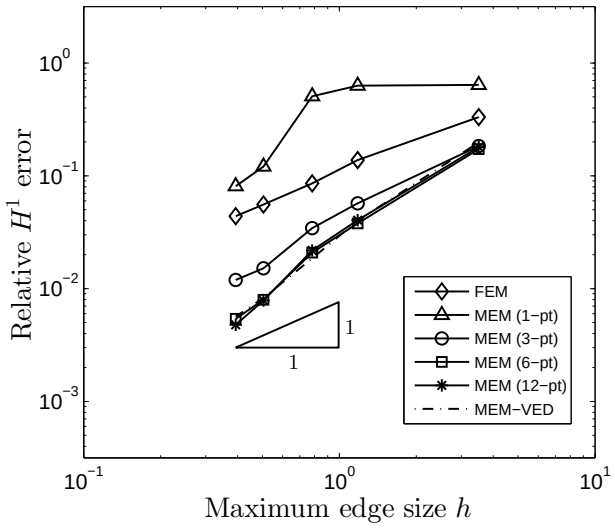

(b)

Figure 15: Rates of convergence for the pressurized thick-walled cylinder problem. Optimal rates of convergence are delivered by the MEM-VED approach in the L^2 norm and the H^1 seminorm. The convergence in the H^1 seminorm is erratic for the MEM approach due to integration errors.

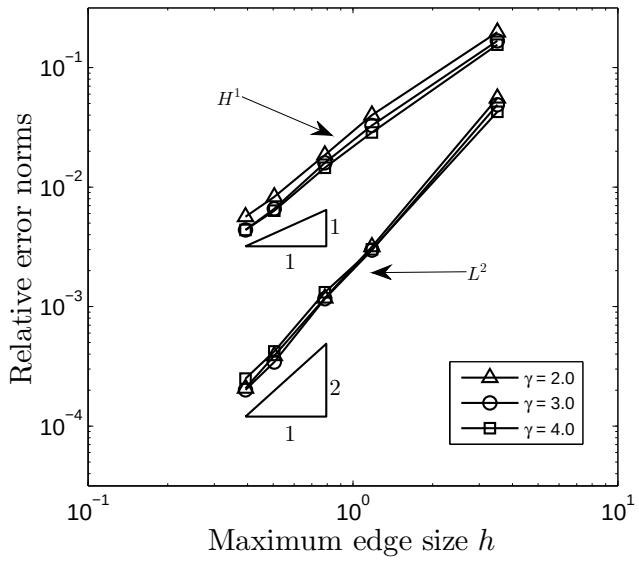

Figure 16: Rates of convergence for the MEM-VED scheme for the problem of a pressurized thick-walled cylinder. Three values for the support parameter γ are chosen in the Gaussian prior weight function. Optimal rates of convergence are obtained for all three cases.

directions, the stratum is cut through the planes $(3, y, z)$ and $(x, y, 3)$, which results in an analysis domain whose dimensions are $3 \times 1 \times 3$. We consider a sequence of unstructured meshes, which is shown in Figure 18. The exact solution for this problem is obtained from Reference [16]:

$$u_x = u_z = 0,$$
$$u_y = \frac{(1+\nu)(1-2\nu)}{E(1-\nu)} \left(-qy - \frac{\rho g}{2} \left(h^2 - (h-y)^2 \right) \right),$$

where the Young's modulus is $E = 4 \times 10^7$ Pa, the Poisson's ratio $\nu = 0.3$, and the density of the stratum is $\rho = 1900$ kg/m^2. The exact solution $u_x = 0$ is applied on the boundary at $x = 3$ and the exact solution $u_z = 0$ on the boundary at $z = 3$. Although the infinite elastic stratum can be readily solved using a one-dimensional model, it illustrates the large errors that are introduced by

the standard Gauss integration in three dimensions.

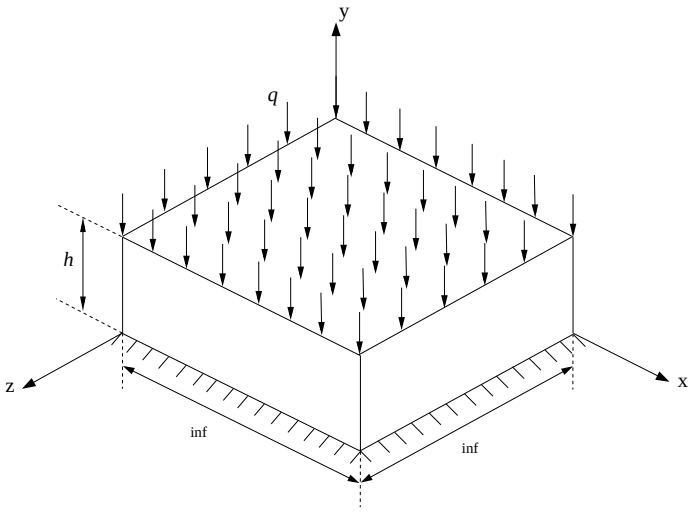

Figure 17: Model geometry and boundary conditions for the infinite elastic stratum problem.

As in the previous examples, the scaling parameter in the stability stiffness is set after performing a sensitivity analysis of α^* in the H^1 seminorm. The background mesh that is shown in Figure 18(c) is used in the analysis. The basis function support parameter is chosen as $\gamma = 2.0$ in the Gaussian prior weight function. The sensitivity analysis is shown in Figure 19, where a minimum is attained at around $\alpha^* = 10^{-4}$. Smaller values for α^* give almost the same error. The reference error value for the four-node FE tetrahedron is also shown in the plot. $\alpha^* = 10^{-4}$ is adopted in the remainder of this example.

A study is conducted to compare the convergence rates that are delivered by the MEM using various standard Gauss integration rules and the MEM-VED formulation upon mesh refinement. The basis function support parameter is set to $\gamma = 2.0$ in the Gaussian prior weight function. Figure 20 presents the convergence rates for both the MEM and the MEM-VED approaches, and the four-node FE tetrahedron. It is observed that the optimal rates of convergence are delivered by

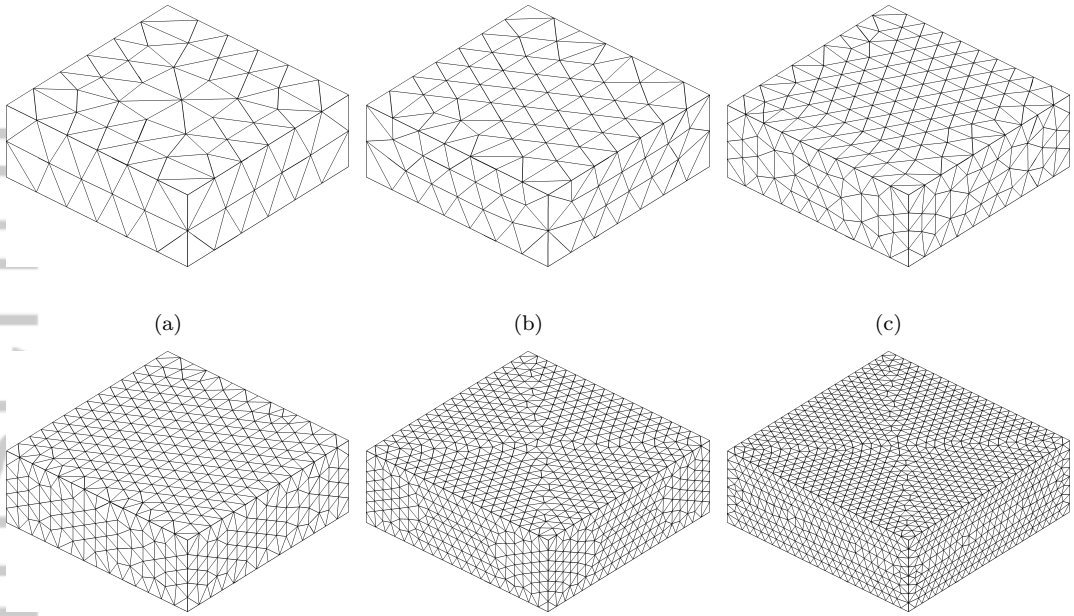

Figure 18: Sequence of background meshes used for the convergence study on the infinite elastic stratum problem.

the MEM-VED formulation in both the L^2 norm and the H^1 seminorm. For the MEM approach, not only is the convergence erratic for the complete sequence of Gauss rules (even a 24-point Gauss rule is inadequate), but it also exhibits poor accuracy. This is a somewhat expected behavior since integration errors are significantly more pronounced in three dimensions [20]; and when comparing the MEM-VED approach with the classical four-node FE tetrahedron, superior accuracy is exhibited by the former. We emphasize that in three dimensions, the MEM-VED formulation only needs a total of four Gauss points to evaluate basis function — derivatives are not needed — on the faces of the cell, which can be exploited for computational efficiency. Figure 21 provides the computational cost of the proposed MEM-VED formulation and the MEM approach using various standard Gauss

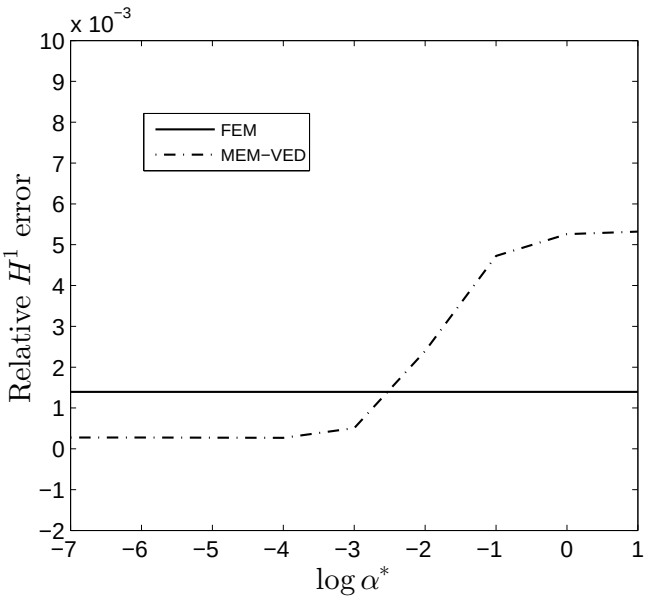

Figure 19: Infinite elastic stratum problem. Sensitivity analysis of α^* in the H^1 seminorm.

integration rules. It is observed that for the same CPU time the MEM-VED approach offers much better accuracy than all the MEM cases. It is also observed that the computational cost of the MEM-VED approach is about the same as the computational cost of the MEM with 4-point standard Gauss rule, but its accuracy is far superior. Hence, this example reveals the better performance of the proposed MEM-VED formulation over the standard MEM approach.

Finally, three values for γ are considered to study the effect of the support size of the nodal basis function in three dimensions. The resulting rates of convergence are provided in Figure 22, where it is observed that the optimal rates of convergence are delivered by the MEM-VED scheme in both the L^2 norms and the H^1 seminorm for all three values of γ.

6.2.6. Numerical stability. To assess the stability of the proposed meshfree method using the virtual element decomposition, eigenvalue analyses are performed in linear elastostatics using the

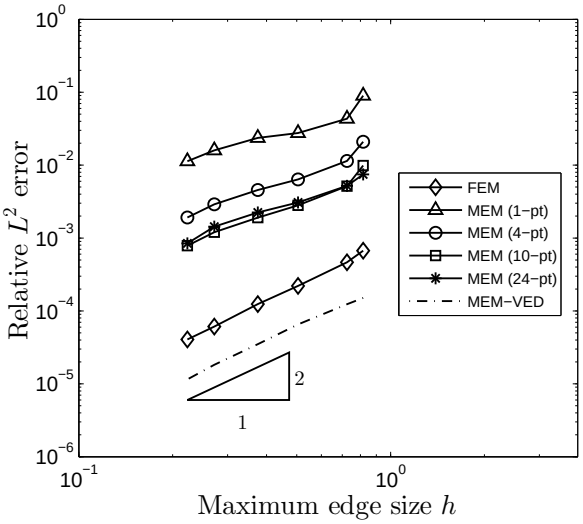

(a)

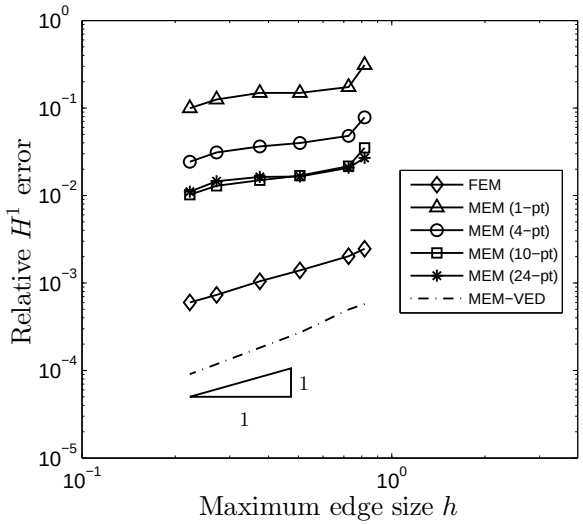

(b)

Figure 20: Rates of convergence for the infinite elastic stratum problem. The MEM-VED method delivers the optimal rates of convergence in the L^2 norm and the H^1 seminorm. For the MEM method, integration errors lead to erratic convergence and poor accuracy.

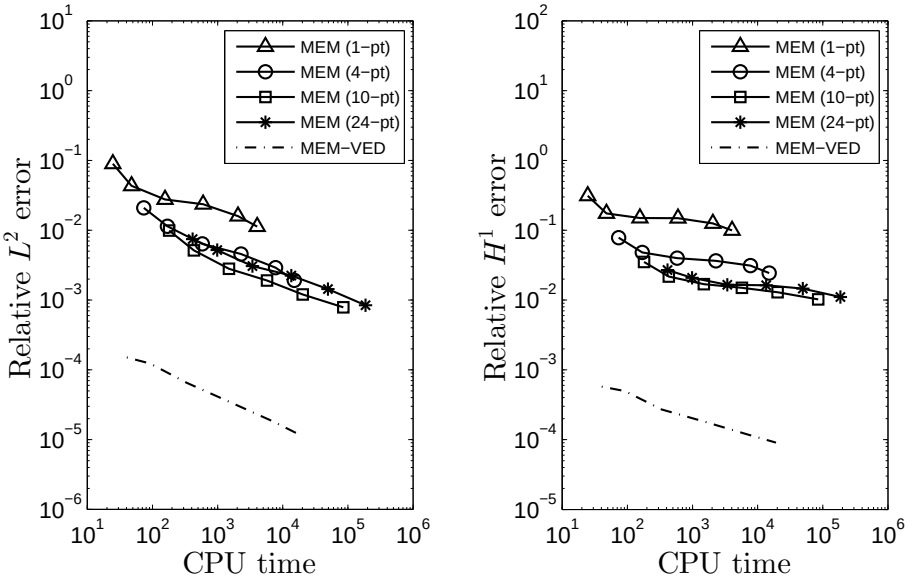

(a) (b)

Figure 21: Computational cost of the meshfree schemes in the infinite elastic stratum problem. The computational cost of the MEM-VED approach is about the same as the computational cost of the MEM with 4-point standard Gauss rule, but its accuracy is far superior.

data of the infinite elastic stratum problem (see Section 6.2.5). The basis function support parameter is chosen as $\gamma = 2.0$. The three-dimensional eigenvalue analyses deliver six zero eigenvalues for both the MEM and MEM-VED methods, which correspond to the six normal rigid body modes. The three mode shapes that follow the six rigid body modes are depicted in Figure 23. Figures 23(a)–(c) depict the mode shapes for MEM with 1-point Gauss rule and Figures 23(d)–(f) for MEM with 24-point Gauss rule. Although the sixth and seventh mode shapes look smooth for both MEM cases, the stability issue due to integration errors in the standard Gauss integrated stiffness appears in the ninth mode. In stark contrast, Figures 23(g)–(i) show the smooth mode shapes that are obtained

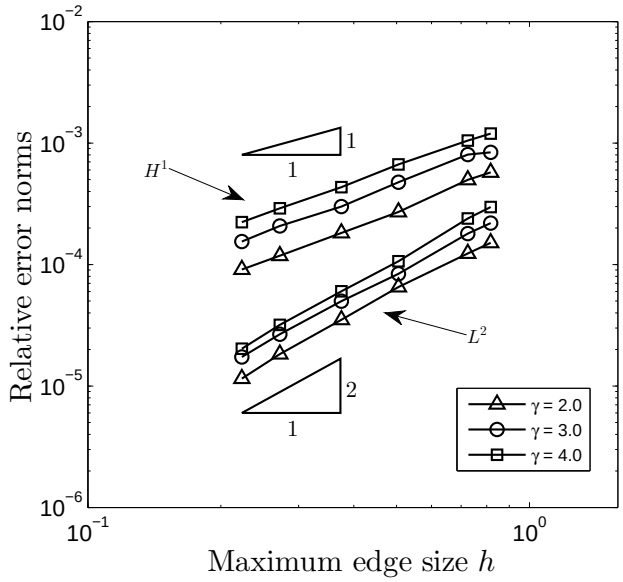

Figure 22: Rates of convergence of the MEM-VED method for the infinite elastic stratum problem. Three values for the support parameter γ are chosen in the Gaussian prior weight function. The MEM-VED approach delivers the optimal rates of convergence for all three cases.

in the MEM-VED approach.

7. CONCLUDING REMARKS

In this paper, a new methodology for meshfree Galerkin methods that precludes integration errors was presented. Maximum-entropy meshfree basis functions were adopted, and the stability and consistency of the numerical solution are inherited by appealing to the virtual element decomposition [3]. We referred to this new approach as MEM-VED. In the MEM-VED formulation, a new stiffness matrix is realized as the summation of a consistency stiffness and a stability stiffness. The stiffness matrix is then used in the weak form. Several numerical examples were presented for

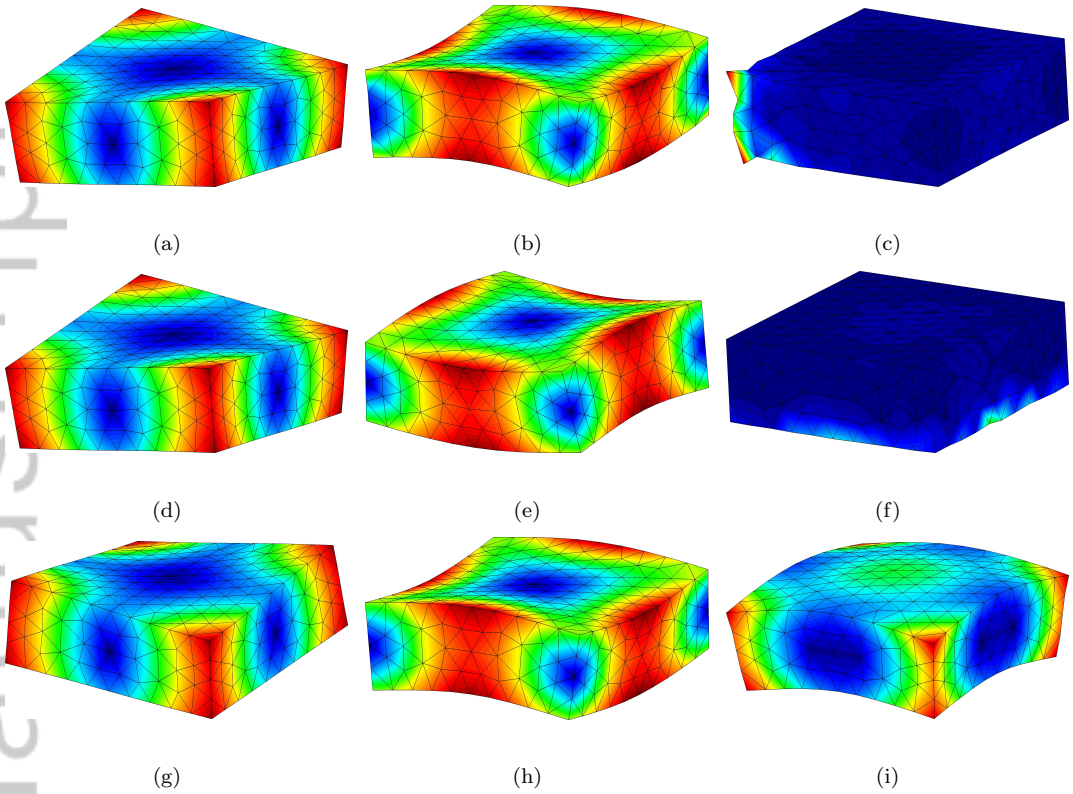

Figure 23: Three dimensional eigenvalue analyses. Depiction of the three mode shapes that follow the six rigid body modes. (a)-(c) MEM (1-pt), (d)-(f) MEM (24-pt), (g)-(i) VEM-VED.

the Poisson and linear elastostatic problems using Delaunay tessellations (three-node triangles and four-node tetrahedra) as background cells for numerical integration of the stiffness matrix.

The numerical examples were tailored to compare the performance of the MEM-VED approach and the standard MEM. In the MEM-VED formulation, the integration of the consistent and stability stiffness matrices requires 1-point Gauss rule per face of the cell and only involves the evaluation of basis functions (no derivatives are needed); and due to the particular choice adopted in the construction of the stability stiffness in the Poisson problem, an additional 1-point Gauss

rule in the interior of the cell is required for the integration of this stiffness. The numerical results reveal that only the MEM-VED approach provides patch test satisfaction to machine accuracy.

In the standard MEM, the convergence rates are problem dependent as summarized as follows: in the two-dimensional Poisson problem, 3-point Gauss rule was required to obtain the optimal rate of convergence in the L^2 norm and 12-point Gauss rule for optimal convergence in the H^1 seminorm; in the cantilever beam problem, 3-point Gauss rule was required to obtain the optimal rate of convergence in the L^2 norm and 6-point Gauss rule for optimal convergence in the H^1 seminorm; in the two-dimensional pressurized thick-walled cylinder, 6-point Gauss rule was needed to obtain the optimal convergence rates in both the L^2 norm and H^1 seminorm. In three dimensions, the inaccuracies that are introduced by the quadrature errors were manifested by large errors and erratic convergence — even an expensive 24-point Gauss rule proved to be insufficient. On the other hand, the MEM-VED formulation delivered the optimal rates of convergence in two and three dimensions. Finally, we conducted numerical eigenvalue analyses to establish the stability of the three-dimensional MEM-VED formulation.

APPENDIX A: ON THE CHOICE FOR THE PROJECTION OPERATOR

We briefly explain the particular form of the projection operator chosen in the Poisson problem. The procedure is given in Reference [31]. We start by showing that (17a) can be obtained from (15). Since $p \in \mathcal{P}(E)$, its gradient is a constant vector, and therefore (15) becomes

$$|E| \boldsymbol{\nabla} p \cdot \boldsymbol{\nabla} \Pi u = \boldsymbol{\nabla} p \cdot \int_E \boldsymbol{\nabla} u \, d\boldsymbol{x}. \tag{46}$$

The constant part of p leads to the equality $0 = 0$ in (46) (and thus in (15)) leading to its indeterminancy. To fix this, we first consider the linear monomials $p_1 = \{x_1 \quad x_2 \quad x_3\}^{\mathrm{T}}$ and the

constant monomial is treated separately. On replacing $p = p_1$ into (46) and applying the divergence theorem yields

$$\boldsymbol{\nabla} \Pi u = \frac{1}{|E|} \int_E \boldsymbol{\nabla} u \, d\boldsymbol{x} = \frac{1}{|E|} \int_{\partial E} u \boldsymbol{n} \, dS = g(u). \tag{47}$$

Hence, the following projection verifies (47):

$$\Pi u = \boldsymbol{x} \cdot \boldsymbol{g}(u) + c, \tag{48}$$

where c is a constant function that depends on u. This means that (48) is defined up to a constant and explains why the constant monomial needs to be treated separately. To find c, we need a projection operator onto constants defined as

$$\Pi_0 : \mathcal{W}(E) \to \mathbb{R}, \quad \Pi_0 \left(\Pi u - u \right) = 0 \quad \forall u \in \mathcal{W}(E). \tag{49}$$

A typical choice for Π_0 is given by [31]

$$\Pi_0 u = \frac{1}{N} \sum_{J=1}^{N} u(\boldsymbol{x}_J), \tag{50}$$

which is the same as the mean value of u over the vertices of the integration cell computed through (12). Now, we apply (49) to (48) to obtain:

$$\Pi_0(\Pi u) = \Pi_0(\boldsymbol{x}) \cdot \boldsymbol{g}(u) + \Pi_0 c = \Pi_0 u. \tag{51}$$

Due to the definition of Π_0 in (50) and that c is a constant function, $\Pi_0 c = c$. Also, $\Pi_0 u = \bar{u}$ and $\Pi_0(\boldsymbol{x}) = \bar{x}$, where the bared quantities are exactly as defined in (12). By using the preceding equalities, the constant function c can be obtained from (51) as follows:

$$c = \Pi_0 u - \Pi_0(\boldsymbol{x}) \cdot \boldsymbol{g}(u) = \bar{u} - \bar{\boldsymbol{x}} \cdot \boldsymbol{g}(u). \tag{52}$$

Finally, on substituting (52) into (48) leads to

$$\Pi u = (\boldsymbol{x} - \bar{\boldsymbol{x}}) \cdot \boldsymbol{g}(u) + \bar{u}, \tag{53}$$

which is the choice given in (17a).

Equation (53) also satisfies (14) since

$$I\!\!P p_1 = (\boldsymbol{x} - \bar{\boldsymbol{x}}) \cdot \boldsymbol{g}(p_1) + \bar{p_1} = \boldsymbol{I}(\boldsymbol{x} - \bar{\boldsymbol{x}}) + \bar{\boldsymbol{x}} = \boldsymbol{x} = p_1,$$

where $\boldsymbol{g}(p_1) = \boldsymbol{I}$ has been used by virtue of (47).

ACKNOWLEDGEMENTS

NS gratefully acknowledges the research support of the National Science Foundation through contract grant CMMI-1334783 to the University of California at Davis. Helpful discussions with Professor Lourenco Beirão da Veiga are also acknowledged.

REFERENCES

[1] T. Belytschko, Y. Krongauz, D. Organ, M. Fleming, and P. Krysl. Meshless methods: An overview and recent developments. *Computer Methods in Applied Mechanics and Engineering*, 139:3–47, 1996.

[2] V. P. Nguyen, T. Rabczuk, S. Bordas, and M. Duflot. Meshless methods: A review and computer implementation aspects. *Mathematics and Computers in Simulation*, 79(3):763–813, 2008.

[3] L. Beirão da Veiga, F. Brezzi, A. Cangiani, G. Manzini, L. D. Marini, and A. Russo. Basic principles of virtual element methods. *Mathematical Models and Methods in Applied Sciences*, 23(1):199–214, 2013.

[4] J.-S. Chen, M. Hillman, and M. Rüter. An arbitrary order variationally consistent integration

for Galerkin meshfree methods. *International Journal for Numerical Methods in Engineering*, 95(5):387–418, 2013.

[5] I. Babuška, U. Banerjee, J. E. Osborn, and Q. L. Li. Quadrature for meshless methods. *International Journal for Numerical Methods in Engineering*, 76(9):1434–1470, 2008.

[6] I. Babuška, U. Banerjee, J. E. Osborn, and Q. Zhang. Effect of numerical integration on meshless methods. *Computer Methods in Applied Mechanics and Engineering*, 198(37–40):2886–2897, 2009.

[7] Y. Krongauz and T. Belytschko. Consistent pseudo-derivatives in meshless methods. *Computer Methods in Applied Mechanics and Engineering*, 146(2–3):371–386, 1997.

[8] J. S. Chen, C. T. Wu, S. Yoon, and Y. You. A stabilized conforming nodal integration for Galerkin mesh-free methods. *International Journal for Numerical Methods in Engineering*, 50(2):435–466, 2001.

[9] P. Breitkopf, A. Rassineux, J.-M. Savignat, and P. Villon. Integration constraint in diffuse element method. *Computer Methods in Applied Mechanics and Engineering*, 193(12–14):1203–1220, 2004.

[10] B. Nayroles, G. Touzot, and P. Villon. Generalizing the finite flement method: Diffuse approximation and diffuse elements. *Computational Mechanics*, 10(5):307–318, 1992.

[11] A. Ortiz, M. A. Puso, and N. Sukumar. Maximum-entropy meshfree method for compressible and near-incompressible elasticity. *Computer Methods in Applied Mechanics and Engineering*, 199(25–28):1859–1871, 2010.

[12] A. Ortiz, M. A. Puso, and N. Sukumar. Maximum-entropy meshfree method for incompressible media problems. *Finite Elements in Analysis and Design*, 47(6):572–585, 2011.

[13] C. Talischi, A. Pereira, I. F. M. Menezes, and G. H. Paulino. Gradient correction for polygonal and polyhedral finite elements. *International Journal for Numerical Methods in Engineering*, 102(3–4):728–747, 2015.

[14] Q. Duan, X. Li, H. Zhang, and T. Belytschko. Second-order accurate derivatives and integration schemes for meshfree methods. *International Journal for Numerical Methods in Engineering*, 92(4):399–424, 2012.

[15] Q. Duan, X. Gao, B. Wang, , X. Li, H. Zhang, T. Belytschko, and Y. Shao. Consistent element-free Galerkin method. *International Journal for Numerical Methods in Engineering*, 99(2):79–101, 2014.

[16] Q. Duan, X. Gao, B. Wang, X. Li, and H. Zhang. A four-point integration scheme with quadratic exactness for three-dimensional element-free Galerkin method based on variationally consistent formulation. *Computer Methods in Applied Mechanics and Engineering*, 280(0):84–116, 2014.

[17] A. Ortiz-Bernardin, J. S. Hale, and C. J. Cyron. Volume-averaged nodal projection method for nearly-incompressible elasticity using meshfree and bubble basis functions. *Computer Methods in Applied Mechanics and Engineering*, 285:427–451, 2015.

[18] A. Ortiz-Bernardin, M. A. Puso, and N. Sukumar. Improved robustness for nearly-incompressible large deformation meshfree simulations on Delaunay tessellations. *Computer Methods in Applied Mechanics and Engineering*, 293:348–374, 2015.

[19] A. Cangiani, G. Manzini, A. Russo, and N. Sukumar. Hourglass stabilization and the virtual element method. *International Journal for Numerical Methods in Engineering*, 102(3–4):404–436, 2015.

[20] C. Talischi and G. H. Paulino. Addressing integration error for polygonal finite elements through polynomial projections: A patch test connection. *Mathematical Models and Methods in Applied Sciences*, 24(08):1701–1727, 2014.

[21] G. Manzini, A. Russo, and N. Sukumar. New perspectives on polygonal and polyhedral finite element methods. *Mathematical Models and Methods in Applied Sciences*, 24(08):1665–1699, 2014.

[22] S. Beissel and T. Belytschko. Nodal integration of the element-free Galerkin method. *Computer Methods in Applied Mechanics and Engineering*, 139(1):49–74, 1996.

[23] J. Bonet and S. Kulasegaram. Correction and stabilization of smooth particle hydrodynamics methods with applications in metal forming simulations. *International Journal for Numerical Methods in Engineering*, 47(6):1189–1214, 2000.

[24] J. S. Chen, S. Yoon, and C. T. Wu. Non-linear version of stabilized conforming nodal integration for Galerkin mesh-free methods. *International Journal for Numerical Methods in Engineering*, 53(12):2587–2615, 2002.

[25] M. A. Puso, J. S. Chen, E. Zywicz, and W. Elmer. Meshfree and finite element nodal integration methods. *International Journal for Numerical Methods in Engineering*, 74(3):416–446, 2008.

[26] N. Sukumar. Construction of polygonal interpolants: a maximum entropy approach. *International Journal for Numerical Methods in Engineering*, 61(12):2159–2181, 2004.

[27] M. Arroyo and M. Ortiz. Local maximum-entropy approximation schemes: a seamless bridge between finite elements and meshfree methods. *International Journal for Numerical Methods in Engineering*, 65(13):2167–2202, 2006.

[28] N. Sukumar and R. W. Wright. Overview and construction of meshfree basis functions: from moving least squares to entropy approximants. *International Journal for Numerical Methods in Engineering*, 70(2):181–205, 2007.

[29] L. Beirão da Veiga, F. Brezzi, and L. D. Marini. Virtual elements for linear elasticity problems. *SIAM Journal on Numerical Analysis*, 51(2):794–812, 2013.

[30] A. L. Gain, C. Talischi, and G. H. Paulino. On the virtual element method for three-dimensional linear elasticity problems on arbitrary polyhedral meshes. *Computer Methods in Applied Mechanics and Engineering*, 282(0):132–160, 2014.

[31] L. Beirão da Veiga, F. Brezzi, L. D. Marini, and A. Russo. The Hitchhiker's Guide to the Virtual Element Method. *Mathematical Models and Methods in Applied Sciences*, 24(08):1541–1573, 2014.

[32] L. Beirão da Veiga and G. Manzini. A virtual element method with arbitrary regularity. *IMA Journal of Numerical Analysis*, 34(2):759–781, 2014.

[33] S. P. Timoshenko and J. N. Goodier. *Theory of Elasticity.* McGraw-Hill, NY, third edition, 1970.

[34] A. F. Bower. *Applied Mechanics of Solids.* CRC Press, Taylor and Francis Group, Boca Raton, FL, 2010.